Ocean Sci., 11, 215–236, 2015
www.ocean-sci.net/11/215/2015/
doi:10.5194/os-11-215-2015

Ocean Science
Open Access

Temperature–salinity distribution in the northeastern Atlantic from ship and Argo vertical casts

I. Bashmachnikov[1,2], F. Neves[1], Â. Nascimento[1], J. Medeiros[1], I. Ambar[1,2], J. Dias[1,2], and X. Carton[3]

[1]MARE – Marine and Environmental Sciences Centre/ Centro de Oceanografia, Faculdade de Ciências, Universidade de Lisboa, Campo Grande, 1749-016, Lisbon, Portugal
[2]Departamento de Engenharia Geográfica, Geofísica e Energia (DEGGE), Faculdade de Ciências, Universidade de Lisboa, Campo Grande, 1749-016 Lisbon, Portugal
[3]Laboratoire de Physique des Océans, UMR 6523, Université de Bretagne Occidentale, 6 avenue Le Gorgeu, 29200 Brest, France

Correspondence to: I. Bashmachnikov (igorb@fc.ul.pt)

Received: 15 April 2014 – Published in Ocean Sci. Discuss.: 11 June 2014
Revised: 4 October 2014 – Accepted: 4 February 2015 – Published: 5 March 2015

Abstract. The present study defines new interpolation functions for hydrological data. These functions are applied to generate climatological maps of temperature–salinity distribution with a 25 m depth interval and a 30 km space interval (MEDTRANS data set). The data undergo rigorous initial data quality control, having passed several filtering procedures. The gridding is done on neutral density surfaces, which allows better representation of thermohaline fronts for the same gridding radius. The multi-pass Barnes optimum interpolation procedure with spatially variable size of the gridding window is used. The shape of the window accounts for the dominant along-isobath direction of water mass transport over steeply sloping topography. A local ratio of topographic to planetary β-effects is used to define the shape of the window as a function of the relative importance of the topographic influence. The N/f ratio is applied to account for the baroclinic compensation decay of the topographic influence on water mass transport with the distance from the bottom. The gridded fields are available at the website of the Centre of Oceanography of the University of Lisbon (http://co.fc.ul.pt/en/data).

The MEDTRANS climatology gives more details of the distribution of water characteristics in the subtropical northeastern Atlantic than other alternative climatologies and is able to reproduce a number of dynamic features described in the literature: the acceleration in the meanders of the Azores current; the cyclonic gyre in the Gulf of Cadiz; and the splitting and separation of the Mediterranean Water (MW) outflow in two veins near the Gorringe and Galicia banks. Seasonal climatologies, computed for the warm (May–October) and cold (November–April) seasons, reveal stronger zonal extension of the upper ocean patterns during the warm season, as compared to the cold one.

1 Introduction

This work presents detailed maps of climatic temperature–salinity distribution of ocean characteristics in the subtropical northeastern Atlantic (25–45° N and 6–35° W), with special focus on the propagation of the Mediterranean Water (MW).

The subtropical northeastern Atlantic region is dominated by two nearly zonal flows: the southern branch of the North Atlantic Current (SNAC) that crosses the Mid-Atlantic Ridge (MAR) at 45–48° N (Bower et al., 2002), and the Azores Current (AzC) that crosses the MAR at 34–35° N (Klein and Siedler, 1989; Jia, 2000). The 60 km wide jet-like AzC separates the warm and salty tropical water from the subtropical water and its dynamic and thermohaline signal reaches 1000 m depth or more (Käse and Siedler, 1982; Volkov and Fu, 2010). The SNAC separates the subtropical water from the colder and fresher sub-Polar water (Read et al., 2010) and extends over 1000 m. Pollard and Pu (1985) also mention the dominance of the eastward mean drift in the upper 200–300 m layer over the subtropical Atlantic. More recent

studies suggest that the drift is separated into several weak meandering southwestward jets (Paillet and Mercier, 1997).

Near the Iberian and northwestern African coasts, the Portugal Current (PC) and the Canary Current (CC) constitute a system of wide and shallow ocean flows together with coastally trapped upwelling jets (Martins et al., 2002; Perez et al., 2001; Pelegri et al., 2005, Nolasco et al., 2013). Below the coastal jet of the CC, a deeper northward flow, trapped by the African continental slope, transports the Antarctic Intermediate Water (AAIW) as far as the Gulf of Cadiz (Louarn and Morin, 2011). Underneath the PC, the deep poleward flow incorporates the Mediterranean Undercurrent (MUC), which vertically splits into upper and lower cores (Ambar, 1983; Ambar et al., 2008).

Presently there are several global and regional databases covering the study region. The most known is the World Ocean Atlas 2009 (WOA09), where a minimum radius of the gridding window of 444 km is used and the grid resolution is $1^\circ \times 1^\circ$. During the course of this work, the World Ocean Atlas 2013 (WOA13) was being published. The WOA13 has a radius of the gridding window of 214–321 km and a maximum grid resolution of $0.25^\circ \times 0.25^\circ$. It shows a significantly improved climatology in the study region as compared to WOA09. At the same time, the gridding procedure with the radius of influence of more than 200 km significantly oversmoothes the frontal zones, especially near the Iberian continental slope, where the spreading of the MW is characterized by very sharp temperature–salinity gradients. In particular, the MUC is 20–80 km wide and is not adequately reproduced in WOA13 (details are given in Sect. 3). In the present study, the bottom-trapped Mediterranean Undercurrent signature is better reproduced due to the reduction in the local radius of influence to 70 km near the Iberian Peninsula. Additionally, stretching of the gridding window along steep topographic slopes, as well as the use of isopycnic mapping, give advantages in the representation of frontal boundaries, compared to the isobaric mapping used in WOA09 and WOA13. Isobaric mapping is also known to produce artificial temperature–salinity anomalies in the vicinity of frontal zones, which does not happen for isopycnic gridding procedures (Lozier et al., 1994).

Among other climatologies covering the study region, we consider AMA (Roemmich and Gilson, 2009), MIMOC (Schmidtko et al., 2013) and DIVA (Troupin et al., 2010). AMA climatology is based exclusively on ARGO data. The data set does not allow mapping of the MUC along the continental slope of the Iberian Peninsula (as there are very few ARGO floats there). Therefore, it will not be used for comparison. DIVA climatology has too much noise in climatic fields and it will also not be used for comparison. The MIMOC climatology has a $0.5^\circ \times 0.5^\circ$ resolution and is based on isopycnic mapping. We will show below that our results closely correspond to the results of MIMOC in the upper ocean. At the same time, MIMOC has the disadvantage of lower resolution and of the use of sigma surfaces instead of neutral density surfaces. The climatology is also found to produce artifacts in temperature–salinity distributions below 1500 m (see Sect. 3).

Table 1. Profile statistics per instrument type for 25 m vertically binned profiles. Percent good is calculated for both temperature and salinity.

Data type	Number of profiles	> 50 % good	> 75 % good	> 90 % good
CTD	9973	99 %	98 %	96 %
PFL	21634	96 %	96 %	95 %
OSD	22822	96 %	95 %	91 %
Total	54429	97 %	96 %	93 %

Neutral density surfaces (McDougall, 1987), used in this study, are a generalization of the concept of standard σ_n ($n = 0$, 1, 2, etc.) surfaces. The former are parallel to σ_n surfaces at their reference levels.. Along a neutral density surface, a change in density due to saline contraction is compensated for by thermal expansion $\alpha \nabla_n \theta - \beta \nabla_n S = 0$, where α is the thermal expansion coefficient, β is the saline contraction coefficient (both are temperature–salinity–pressure dependent) and the gradient ∇_n is taken along the neutral density surface. Therefore, a particle travelling along a neutral density surface does not experience the effect of the buoyancy force. This is not true for a particle travelling along a σ_n surface (McDougall, 1987).

The methodology of this study (described in Sect. 2) complements the existing gridding methods (WOA09, WOA13, Schmidtko et al., 2013, Troupin et al., 2010) and the resulting climatic fields provide additional details on temperature–salinity distributions (described in Sect. 3). The sufficiently large number of data and their rather even spatial distribution allow us to base the parameters of the gridding procedure on characteristics of local hydrodynamics. This increases the realism of the derived regional circulation patterns. The present climatology is obtained in the framework of project MEDTRANS, and will further be referred to as MEDTRANS climatology.

2 Materials and methods

Data from the World Ocean Database (WOD) were downloaded from the National Oceanographic Data Center (NODC, http://www.nodc.noaa.gov/): CTD (conductivity–temperature–depth, high vertical resolution of typically 1 m or less) and PFL (profiling float, medium vertical resolution of typically 1–10 m, mainly obtained from the ARGO profiling float array), and OSD (ocean station data, low-vertical resolution of typically more than 10 m) from 1950 to 2011.

Bathymetry data, used for conditioning of some data filters and for gridding procedures, are obtained from

the ETOPO2 data set (http://www.ngdc.noaa.gov/mgg/fliers/01mgg04.html).

Within the study region, there are over 54 000 profiles (Table 1). The spatial distribution densities of CTD (and to a lesser extent of OSD) profiles show a tendency to decrease from the continental margin seawards. The PFL profiles cover the region rather uniformly, but mostly the areas away from the continent and with water depth exceeding 1000 m. A large number of the OSD data are concentrated along standard sections, such as the WOCE A03 section (around 36° N), WOCE AR21/A16 sections (around 20 and 25° W), Portugal–Greenland sections, etc. OSD data mostly cover the years 1970–1995 (with a maximum number of casts between 1985 and 1990), CTD data for 1985–2000 (with a maximum number of casts between 1990 and 1995), and PFL for 2000–2011 (with a maximum number of casts after 2005). The climatic maps are constructed under a priori assumption of no strong interannual variations of water properties in the region since 1950. If not, local biases of the final climatology may emerge. Seasonal biases should not arise, since the data are rather homogeneously distributed across the seasons in any part of the region.

A quality control procedure was applied to all z level profiles from the NODC data set, attributing different flags to the data points according to their quality. The first step consists in screening for major instrument malfunctions or calibration errors. This consists in verifying whether vertical temperature–salinity profiles significantly deviate from the WOA09 climatological profiles interpolated to the observed profiles' positions. Assuming normal distribution of temperature–salinity deviations from climatology at any depth level, a profile is considered to be bad if the whole profile deviates from the climatological mean profile by more than 5 standard deviations. Mean standard deviations of 0.07 for salinity and 0.35 °C for temperature, derived from the WOA09 data set, form the criteria. If only a part of the profile deviates from the WOA09 over 5 standard deviations, the profile is considered "dubious" and the data reliability is verified by eye-checking. The expert decision is made based on persistence of the same dubious structures in other local profiles. This filter is not applied for the upper 100 m layer and the MW layer (700–1500 m), since extreme natural deflections from the WOA09 climatology in those layers significantly exceed the 5 mean standard deviations used as the filtering criterion.

The next step consists of testing the profiles for static stability. In the parts of the profiles where a density inversion exists and exceeds 0.02 kg m^{-3} over a less than 200 m depth range, an attempt to correct the inversion by removing spikes in temperature or salinity is made. For all cases we tend to correct first the salinity spikes, since salinity is typically more vulnerable to observational errors, and then, if necessary, the temperature spikes. Whenever the correction leads to an increase in local standard deviation around the spike in either temperature or salinity, the correction is not applied.

The portions of the profiles treated as "bad" are blanked. If a data gap exists only in the temperature or in the salinity profile, and its size does not exceed 200 m, the gap is linearly (low-resolution OSD) or polynomially (CTD and PFL) interpolated. In the latter case a piecewise cubic Hermite polynomial interpolation is used. This interpolation produces a resulting profile differentiable to the second order, which preserves its extremes and does not suffer from overshooting in the vicinity of abrupt variations in the rate of vertical change in a measured property. Whenever the vertical extension of a gap exceeds 200 m, no interpolation is performed. Also, no extrapolation is performed at the profile edges. All the "good" profiles are reduced to the standard vertical resolution of 25 m.

The results show that 96 % of the casts contained at least 50 % good values for both temperature and salinity, and 93 % of the casts contained at least 90 % good values (Table 1). For some selected depth levels, distributions of the data points that have passed the filtering procedure are presented in Fig. 1a–c. In the upper 1900 m layer, the data are rather uniformly distributed (Fig. 1a–b), while below 2000 m, the absence of PFL data results in less dense area coverage with observations (Fig. 1c–d). Accordingly, the vertical profile of the number of valid data over the study region shows a rapid decrease below 1900 m (Fig. 1d). OSD data form maxima of data concentration at the standard oceanographic levels (Fig. 1d).

Mediterranean Water eddies (meddies) form exceptionally pronounced temperature and salinity anomalies in the mid-ocean in the study region, up to 4 °C and 1, respectively (Richardson et al., 2000), and intensive sampling of one such structure adds a strong local bias to the climatic fields. The casts across meddies are detected using Richardson's criterion (Richardson et al., 1991), i.e. a cast is considered to pass through a meddy when a salinity anomaly of more than 0.2 over a layer of at least 200 m is detected in the depth range between 500 and 1500 m. Those casts are eliminated, together with the surrounding profiles, within 50 km spatial and 30-day time ranges, which may be influenced by the meddy cores. The MUC also forms a strong local temperature–salinity anomaly relative to WOA09 climatology, since this dynamic feature is not correctly represented in WOA09. To avoid confounding the MUC with meddies, the slope region off Iberia with depths less than 2500 m is excluded from this latter filtration. Removing the meddy-related bias, we remove fewer than 4 % of the profiles.

Plotting distributions of temperature–salinity anomalies (relative to WOA09 climatology) for different depth levels, we found consistent positive temperature and salinity anomalies in OSD profiles along some XCTD routes, especially noticeable below the 1500 m level. This feature is not observed for CTD or PFL profiles in the same areas and is presumably due to drawbacks in algorithms for estimation of the depth of XCTD instruments (Levitus et al., 2008). To evaluate the effect, temperature and salinity deviations of the OSD pro-

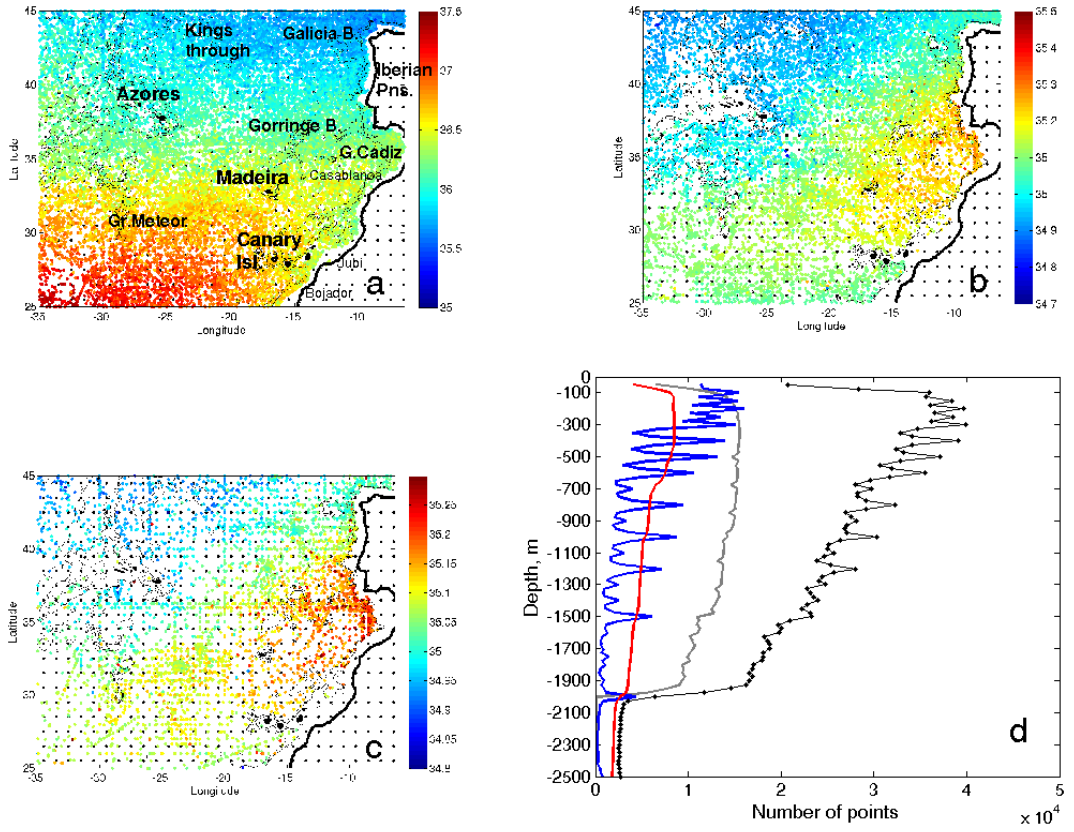

Figure 1. Scatterplot of valid temperature–salinity data points at **(a)** 100 m, **(b)** 1900 m, **(c)** 2000 m, and **(d)** the vertical profile of the number of valid temperature–salinity data points. The WOA09 grid is shown in panels **(a–c)** with black dots. In panels **(a–c)**, the colour scale represents salinity. In panel **(d)**, the black line with markers is the total number of data points; grey line – PFL data only; red line – CTD data only; blue line – OSD data only.

files from WOA09 between 1500 and 2000 m are summed in each of the 100×100 km areas. For a normal distribution of the data deviations from climatology, we expect the sum of the deviations to be close to zero, at least within the limits $\pm 1.96n \times \left(\mathrm{SD}/\sqrt{n}\right)$, where n is the number of data points and SD is the mean standard deviation of temperature–salinity from climatology (see above). For the typical $n = 30$, we exclude OSD casts whenever the sum of the deviations from WOA09 climatology exceeds 1 in salinity or 4 °C in temperature.

In addition, consecutive profiles of a PFL (an Argo float) are removed when a degradation of the salinity sensor with time is noticed. Sensor degradation is detected whenever two criteria are satisfied. Firstly, at the end of the registered float's trajectory, the salinity values show a persistent decrease with time. Secondly, the salinity values differ from a reference value to more than 5 climatic standard deviations. As the reference salinity, we used the mean salinity computed from the other PFL observations in the same area during the period of the possible sensor degradation. If there are no PFL data available, the WOA09 climatology is used as the reference.

The filtered data undergo a gridding procedure. The gridding is done on neutral density surfaces (McDougall, 1987; Jackett and McDougall, 1997). For this study, pressure, temperature and salinity distributions are obtained on 53 neutral density surfaces (G)[1]. The G surfaces are selected to be fairly uniformly distributed in depth, keeping the mean distance between the surfaces less than 50 m in the upper 1500 m layer, and less than 100 m below. In the upper 100 m layer, water stability is generally low, impeding robust computation of neutral density surfaces. In this layer, the isopycnal gridding is substituted by isobaric gridding (Gouretski and Kolterman, 2004).

After calculation of the neutral density surfaces, an additional filter is applied. The computed depth of a neutral density surface can change from one cast to another by as much

[1]The neutral density surfaces used are: 25.50, 25.60, 25.80, 26.00, 26.20, 26.40, 26.60, 26.70, 26.80, 26.90, 26.95, 27.00, 27.05, 27.10, 27.15, 27.20, 27.25, 27.30, 27.35, 27.40, 27.45, 27.50, 27.52, 27.54, 27.56, 27.58, 27.60, 27.62, 27.64, 27.66, 27.68, 27.70, 27.72, 27.74, 27.76, 27.78, 27.80, 27.82, 27.84, 27.86, 27.88, 27.90, 27.92, 27.94, 27.96, 27.97, 27.98, 27.99, 28.00, 28.01, 28.02, 28.03, and 28.04.

as 50–400 m within a few dozens of km. This can be due to a jet-like mean current, as well as due to remnant instrumental errors and eddy noise. Azimuthal velocities and their gradients in eddies are typically higher than velocities and velocity gradients in mean currents; therefore, even when the characteristic length scales of both dynamic structures are the same, eddies generally deflect isopycnic surfaces more strongly than the mean currents. This difference can be used to design a filter.

Removing points with along-isopycnal pressure gradient over some critical value limits the vertical variation in velocity ($\Delta_z V$) across a G surface:

$$\frac{\Delta_z V}{\Delta z} = \frac{N^2}{f}\frac{\partial Z_G}{\partial l},$$

where N is the buoyancy frequency, f is the Coriolis parameter, and l is the direction along the G surface and Z_G is the depth of the G surface. Taking $N^2 = 5 \times 10^{-5}\,\mathrm{s}^{-1}$ and $\frac{\partial Z_G}{\partial l}$ less than 200 m per 200 km, we filter the variations of $\Delta_z V$ that exceed $5\,\mathrm{cm\,s}^{-1}$ per $\Delta z = 100$ m. This value of $\frac{\partial Z_G}{\partial l}$ is taken as the critical one. For comparison, the current velocity gradients in the AzC are observed to be less than $3\,\mathrm{cm\,s}^{-1}$ per 100 m (Comas-Rodriguez et al., 2011). On the other hand, about 100 km downstream from the Strait of Gibraltar, the vertical velocity gradient of the MUC, at its upper boundary, reaches $30\,\mathrm{cm\,s}^{-1}$ per 100 m (Baringer and Price, 1997). Those vertical gradients are observed only within a distance of 10 km from the Iberian continental slope. Over the desired 30 km grid resolution of our study, the mean vertical gradients in the MUC drop to $12\,\mathrm{cm\,s}^{-1}$ per 100 m. To account for those vertical variations, towards the Iberian Peninsula and in the Gulf of Cadiz, the $\frac{\partial Z_G}{\partial l}$ criterion is gradually relaxed to $\Delta_z V$ less than $15\,\mathrm{cm\,s}^{-1}$ per 100 m.

The previous analysis (see also Table 1) gives evidence that the CTD and the PFL profiles have, in general, higher quality than the OSD ones. This is a result of the generally lower quality of sensors and the overall lower vertical resolution of the latter data. Therefore, in the subsequent gridding procedure, the OSD profiles enter with the lower weight of 1, while CTD/PFL data enter with the weight of 2.

The maps of water characteristics are gridded to the Mercator projection used by AVISO altimetry (AVISO). In the study region, the grid has 0.33° resolution in latitude and variable resolution (around 0.30°) in longitude. An advantage of this mesh is that it allows straightforward comparison or merging of the dynamic depths obtained from in situ data with the free-surface topography available from satellites. The same gridding procedure (see below) is applied for isopycnal and isobaric gridding.

Following WOA methodology, we used the Barnes interpolation procedure for gridding scattered observations to a regular mesh (Barnes, 1964). At a grid point ij, the Barnes interpolation value (F_{ij}) is a weighted sum of temperature or salinity values C_s in observational points s situated inside a certain gridding radius. In the original version of the algorithm, the weights are Gaussian functions of distance r_{ijs} between a grid point ij and a data point s (Fig. 2a):

$$W_{ijs} = e^{-r_{ijs}^2/R^2},$$

where R is the e-folding scale (85 % of influence of data points are within $r_{ijs} \le R$). The first-guess gridded fields are formed as

$$F_{ij}^0 = s : |s - ij| < R \sum W_{ijs} C_\mathrm{s} / \sum_s W_{ijs}.$$

Then F_{ij}^0 is interpolated to the positions of the original data points (F_{ijs}^0) and is refined by the iterative procedure

$$F_{ij}^k = F_{ij}^{k-1} + \sum_{s:\ |s-ij|<R} W_{ijs}\left(C_\mathrm{s} - F_{ijs}^{k-1}\right) / \sum_s W_{ijs}.$$

The iterative process increases the steepness of the interface between the no-pass/pass wavelength domains of the filter, i.e. the sharpness of the resulting frontal zones. Thus, the response function of the first-guess gridded field is $D_0 = e^{-(\pi R/\lambda)^2}$, where wavelength λ is the independent variable. The following iterations decrease the span between the fully filtered and fully accepted wavelengths in the response function as (Barnes, 1964)

$$D_k = D_0 \sum_{n=1}^{k} (1 - D_0)^{n-1}.$$

A few modifications to the form of the weight function, introduced in this paper, are listed below.

Potential vorticity conservation constrains the direction of quasi-geostrophic ocean flows, in particular, by steering them along topography (Pedlosky, 1987). The inclination of a bottom slope, necessary for effective trapping of the flow, depends on the local ratio of planetary to topographic β-effects. In the absence of friction, the depth-integrated flow is non-divergent (geostrophic) when

$$v\,\beta/f - \boldsymbol{V} \cdot \nabla H/H = 0. \quad (1)$$

Here the β-plane approximation is used ($f = f_0 + \beta y$), ∇H is the bottom slope, H is the mean water depth, $\boldsymbol{V}$ is the horizontal velocity vector, and v is its meridional component. At the points where the topographic β-effect dominates over the planetary effect, following Schmidtko et al. (2013), we stretch the Gaussian weight function (W_{ijs}) along isobaths. A methodological novelty in this paper is that, using Eq. (1), the algorithm automatically selects the degree to which the topographic β-effect distorts the circular distribution of the isolines of the weight function W (here and further on, indices ijs are omitted).

The resulting weight function is defined as

$$W = [w\,c\,A_\mathrm{h} + (1 - c)]\,e^{-\left(r^2/R^2\right)} \quad (2)$$

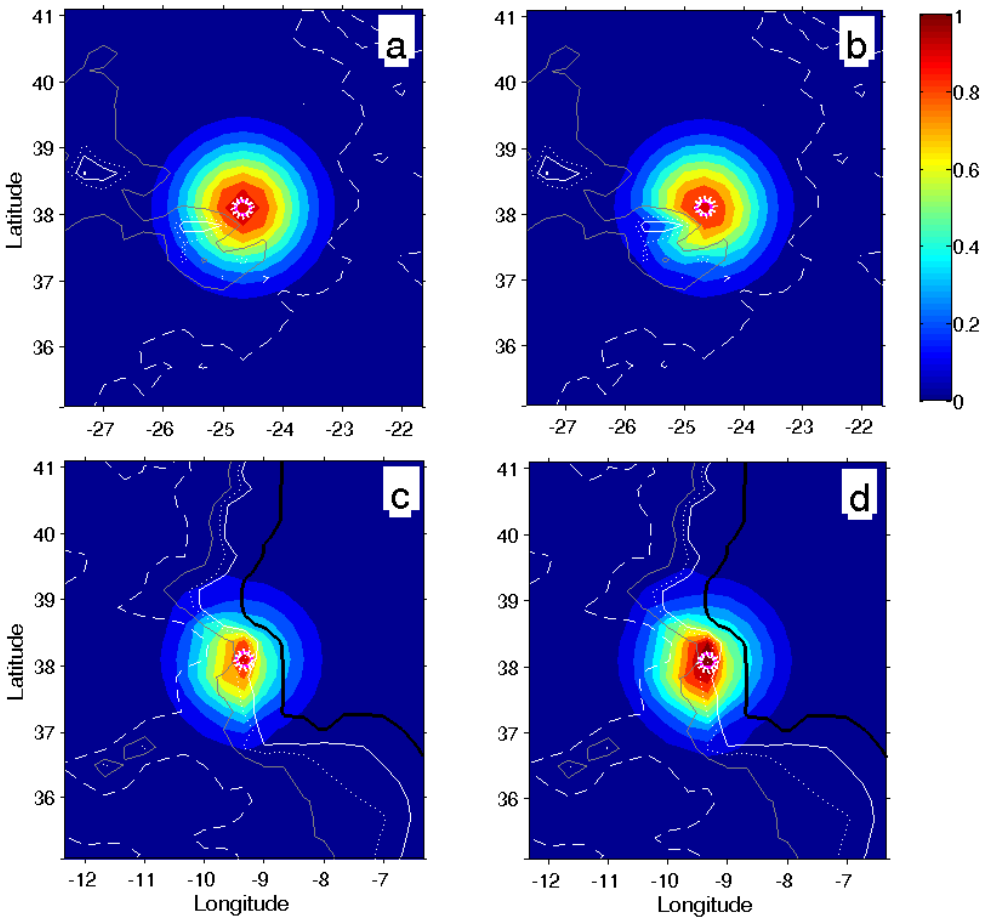

Figure 2. Weight function (W) for **(a)** the small effect of topography for $h = 100$ m, **(b)** the stronger effect at the same location for $h = 1500$ m and **(c–d)** the dominating effect of topography near the continental slope for $h = 100$ m. Lower panels show the shape of the weight function **(c)** when the correction factor w is not applied, and **(d)** with the correction factor w applied. The color scale marks the distribution of the weights as a function of the distance from the central grid point (marked with the white ring). Topographic contours of 0, 500, 1000, 2000, 3000 and 4000 m are presented for reference.

The depth-dependent function A_h is taken to be similar to the one used by Schmidtko et al. (2013):

$$A_\mathrm{h} = \max\left(0.5, \left|1 - 0.5\left|\log\frac{H_{ij}}{H_\mathrm{s}}\right|\right|\right).$$

The function is dependent on water depth variation between the data point (H_s) and the grid point (H_{ij}). The parameter $c = \delta\left(\nabla H/H\right)/\left(\beta/f\right)$ characterizes the relative role of the topographic β-effect relative to the planetary β-effect. The possible variations of the parameter are limited to the range from 0 (no influence of bathymetry) to 1 (the maximum influence of bathymetry). The parameter w (see below) accounts for compensation for the detected decrease in the area of the gridding window over steep topographic slopes. The ETOPO2 bathymetry used is smoothed over the distances of about half of the gridding window radius R (defined below).

Another novelty of the method is that we account for the effect of ocean baroclinicity, i.e. the weakening of the bottom slope effect on the circulation with the distance from the topography. The parameter $\delta = \max\left(0, 1 + \frac{h - H_{ij}}{H_m}\right)$, which is a function of the difference between the gridding level h and the water depth in the grid point (H_{ij}), accounts for this effect. The distance from the bottom, where the bottom influence becomes insignificant on ocean circulation, can be roughly estimated from the expression $H_m \sim L\frac{f}{N}$ (Ownes and Hogg, 1980). With the ratio $\frac{N}{f} \sim 80$–90 (derived from the WOA09 data set), characteristic of the upper 2000 m layer, and the spatial scale $L \sim 200$ km, which is close to the typical width of the major ocean currents, we get $H_m = 2200$–2500 m. The latter value is used for computations (Fig. 2b–d).

It is noted that the expression (Eq. 2) applied over steep topographic slopes strongly reduces the area with high weights (Fig. 2c, with $w = 1$). In areas of very steep bottom slopes (continental margins, banks or seamounts), the resulting mean weight over the gridding window may decrease by as much as 30 %, increasing the noise level of the gridded cli-

matology near the topography. Farther on, this noise manifests itself in strong divergence of the computed geostrophic flows, for example. To avoid this effect, the parameter $w \leq 1$ is introduced as the ratio of the mean weight inside the gridding window (Eq. 2) with locally computed c to the mean weight with $c = 0$. Use of this parameter in the expression (Eq. 2) increases the weights within the gridding window, not affecting the mean gridding radius (Fig. 2d).

When friction is taken into account, the right-hand side of the equation (Eq. 1) is not zero, but includes the effect of the atmospheric wind torque, bottom frictional torque and the joint effect of baroclinicity and bottom relief (JEBAR) (Kantha and Clayson, 2000). In the ocean, the JEBAR is generally small compared to other terms. The bottom frictional torque is efficient only near topography and its effect on the flow results in a gradual change in the mean depth and/or the thickness of a bottom trapped flow. The vorticity pumped into the ocean by the wind torque generates Sverdrup circulation, which, in the eastern parts of the ocean, has a meridional component comparable to the zonal one (Pedlosky, 1998). This is confirmed by the current structure in the subtropical northeastern Atlantic derived from in situ observations (Paillet and Mercier, 1997). These considerations suggest that, in the study region, stretching of the weight function in the zonal direction does not give any benefits to the final product. Since the topographic β-effect at the continental slope or at the MAR slopes is several orders higher than the planetary β-effect, topographic steering effects cannot be neglected. Therefore, in this study, the shape of the weight function is only a function of bathymetric slopes.

Finally, to define the weight function (Eq. 2), we need to define the radius R of the gridding window. Two considerations are taken into account. First, water characteristics at every grid point should be obtained by averaging a sufficient number of observations, in order to reduce the remnant noise due to time inhomogeneity of the original data set. A criterion of at least 30 observation points is used, as suggested for obtaining a reasonable estimate of the first moments (Emery and Thomson, 1997). Second, R should be large enough for remnant traces of vortices being filtered out by the gridding procedure. Variation of data density in the horizontal and vertical suggests spatially varying R, as defined below.

Figure 3 shows that, in the upper 1900 m layer, the radii of windows containing at least 30 points increase from the average 30–60 km near the Iberian Peninsula to 60–110 km in the western and southern parts of the study region. On average, over the study region the radius in the upper 1900 m layer is 30–50 km. Below 1900 m, due to a drastic decrease in the number of profiles (Figs. 1d and 3c), the window radius increases and changes from 60–150 km near the Iberian Peninsula to 150–300 km in the western and southern parts of the study region. On average over the study region, R is 100 km at 2000 m depth and 170 km at 2400 m depth.

Mesoscale and submesoscale anomalies of water properties are one of the main sources of noise in climatic data. The effect of eddies is partly removed by the filtering procedures described above. At the same time, some remnant eddy noise still affects the temperature–salinity fields. To reduce this noise further, we chose the radius of the gridding window to exceed the typical eddy radius considerably (Appendix 1). By this criterion, R should significantly exceed the characteristic eddy radius of 30 km and preferably exceed the maximum eddy radius of 50–100 km. The value of 60–70 km looks to be a reasonable compromise between the urge towards the desired spatial resolution and the maximum reduction in the mesoscale noise level.

Combining the information above (Figs. 3 and A1 in the Appendix), we see that, in the upper 1900 m layer in the eastern part of the study region, R is limited by eddy size, while over the rest of the region it is limited by data density. From the 2000 m level down, R should be doubled, everywhere limited by the data density.

To get the highest possible resolution with the decreasing data density away from the Iberian Peninsula, we used spatially varying R. For G less than or equal to 27.96 kg m^{-3} (in the upper 1900 m layer), R increases from 70 km near the Iberian Peninsula to 200 km in the western part of the study region. Downwards, R increases 1.5 times for G from 27.97 to 27.98 kg m^{-3} (in the layer 1900 to 2000 m) and doubles for G greater than or equal to 27.99 kg m^{-3} (below 2000 m). A smooth transition between the areas with the minimum and the maximum radii is assured by gradual variation of R across the study region (Fig. 4a–b). In Fig. 3d, the Barnes response functions, are presented for different R.

Therefore, in the deep ocean, the data set does not permit gridding with a higher resolution than that of WOA13, while above 1900 m an improvement can be achieved.

For neutral density surfaces, the artificial cabelling effect, which results from the spatial averaging during gridding, is tested. These errors are so small that nudging the temperature and salinity values to return to the referred density, as applied by Schmidtko et al. (2013), is not necessary.

Finally, in every grid point, the vertical profiles of temperature and salinity are vertically interpolated into fixed depth levels with 25 m intervals using piecewise cubic Hermite polynomial interpolation. Depths of isopycnals vary across the region, and the chosen set of isopycnals permits the full coverage of the study region down to 2300 m depth.

3 Results

Zonal and meridional sections of temperature and salinity obtained in this paper are presented in Fig. 5. The figure shows that the neutral density surfaces have a rather uniform vertical distribution. Meridional sections of temperature (Fig. 5a–b) show a rapid rise in the isopycnals around 35° N (the AzC), which is observed down to 1700 m. Farther north, a gradual rise in the isopycnals in the upper 500 m layer corresponds to the dominating eastward flow. In Fig. 5a and d,

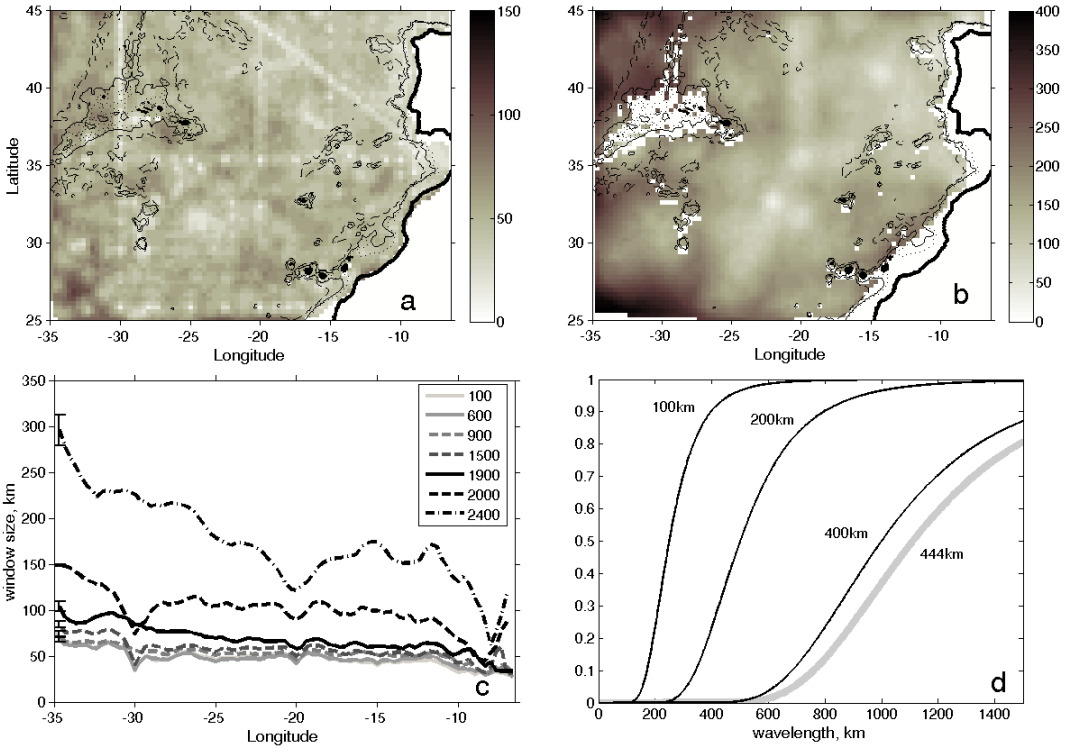

Figure 3. Radius (km) of the window containing a minimum of 30 data points: **(a)** at 100 m and **(b)** at 2500 m depth. Isolines of $R = 100$ km (solid), 200 km (dashed), 300 km (dash–dotted) and 400 km (dotted) are shown. **(c)** Variation of the window size as a function of the distance from the coast and water level. **(d)** Barnes response function for different radii of the window after the third iteration.

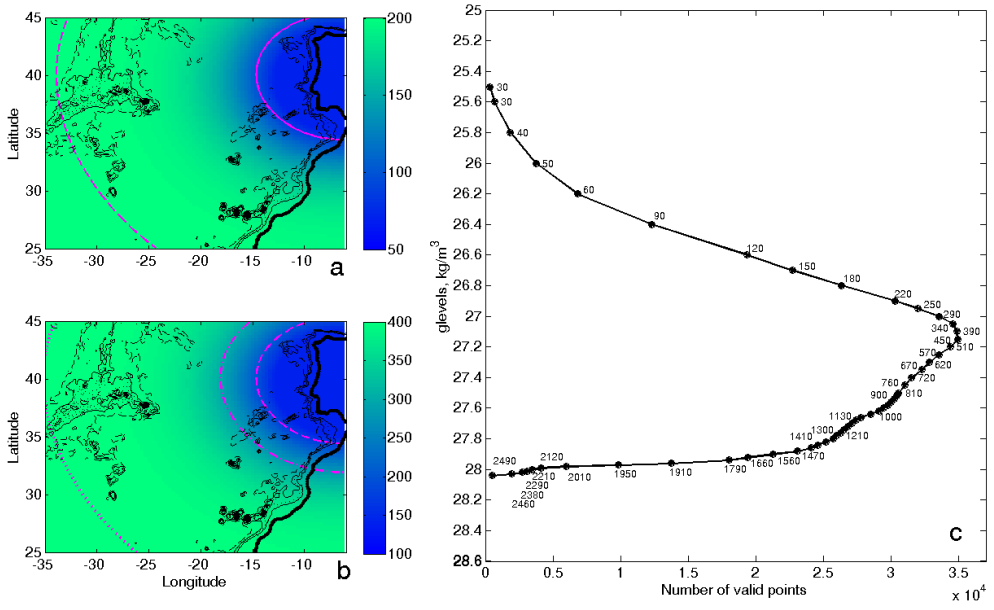

Figure 4. Spatial variation of R in **(a)** the upper 1900 m layer, and **(b)** below 2000 m. Isolines of 100 km (magenta solid), 200 km (magenta dashed), 300 km (magenta dash–dotted) and 400 km (magenta dotted) are added. **(c)** presents the total number of valid salinity data points at the selected neutral density surfaces. The numbers to the right of the black filled circles mark the area-mean depth of the neutral density surface in the study region (not all numbers are presented).

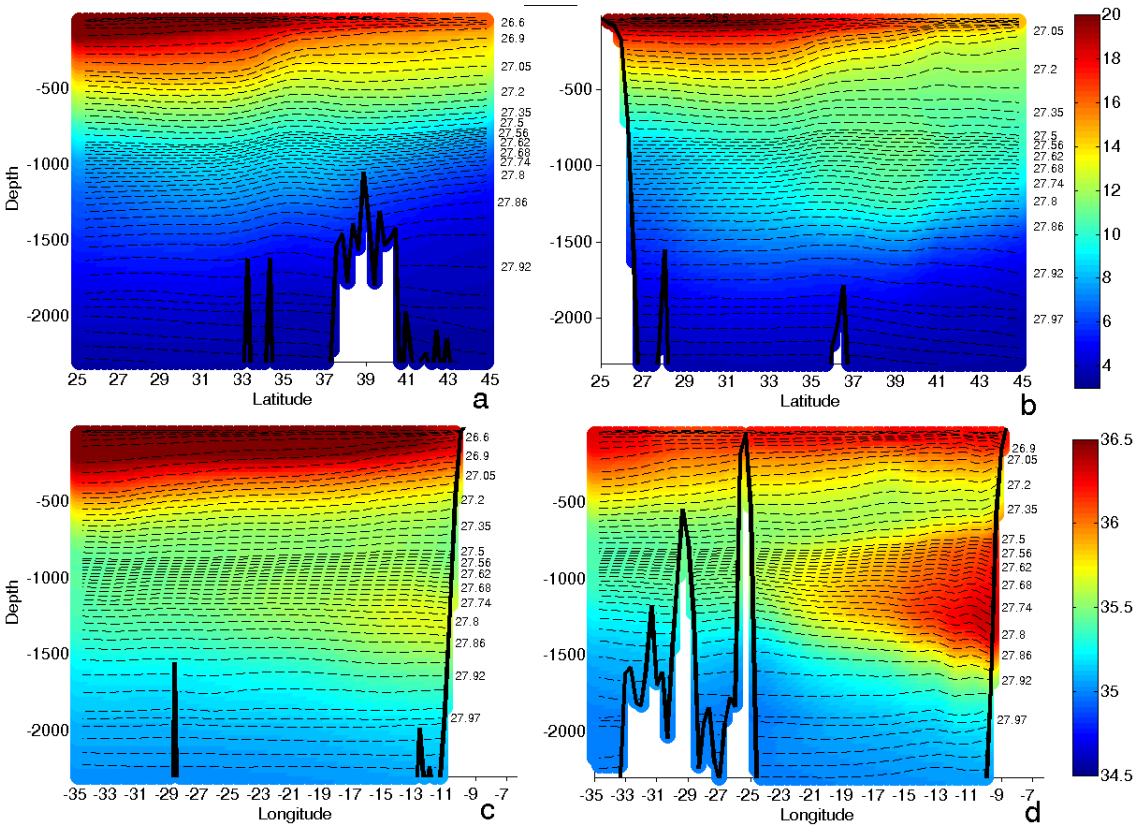

Figure 5. Vertical meridional sections of temperature along **(a)** 30° W and **(b)** 15° W, and zonal sections of salinity along **(c)** 31° N and **(d)** 38° N. The dashed isolines show positions of neutral density surfaces (some of the surfaces are identified to the right of the sections).

one can also observe the isopycnals bending down near the MAR. This should be due to the MAR being a guide for the southward flows along its eastern slope (Bower et al., 2002).

The MW tongue extends from the Iberian Peninsula to the MAR (Fig. 5d). In the vertical, the influence of the MW extends to at least 2000 m (Reid, 1978; Harvey, 1982; Daniault et al., 1994). The colder water plume at the eastern slope of the MAR below 1500 m corresponds to the southward penetration of Labrador Sea Water (LSW) into the eastern subtropical Atlantic (Bower et al., 2002). In the southern part of the region, at 31° N (Fig. 5c), the lower fraction of the MW has the maximum near the African coast between 1000 and 1500 m. The less saline and colder core of the Antarctic Intermediate Water (AAIW) dominates the thermohaline structure along the African coast at around 800–900 m depth (Louarn and Morin, 2011).

3.1 Comparison of annual climatologies

In this section, the temperature–salinity fields of the MEDTRANS climatology, obtained in this paper, are compared to other existing annual climatologies: WOA09, WOA13 and MIMOC (Figs. 6–9).

Figure 7 shows that temperature differences between the climatologies at 600 m do not exceed 1 °C. It is seen that the differences relative to the WOA09 data set are organized in zonally extended patterns (Fig. 7a, b and c). The areas of higher temperature at 600 m (Fig. 7c, f) correspond to the positions of the zonal jets – the branches of the NAC at 40 and 45° N (Maximenko et al., 2008). These zonal jets are seen in MIMOC, but the distribution of the characteristics in the open ocean and coastal zones in MIMOC are over-smoothed as compared to MEDTRANS (Fig. 7a, e, d and g). The MEDTRANS climatology also shows a much sharper frontal zone of the AzC than the MIMOC or WOA09 climatologies. Fewer differences are observed with WOA13. Compared to WOA13, the MEDTRANS climatology presents more details of the upper MW core spreading along the Iberian Peninsula, especially at its southern coast (Fig. 7g, h and i).

Figure 8 presents the salinity distribution at 1200 m, the typical depth of the lower MW core. The differences between the climatologies do not exceed 0.1. The MEDTRANS climatology brings significantly more details on the shape of the MW tongue than the WOA09 or MIMOC ones. In particular, the zonally extended MW maximum between 30 and 33° N, from the Madeira archipelago to the Cruiser–Great Meteor seamounts (30–33° N), is seen with higher

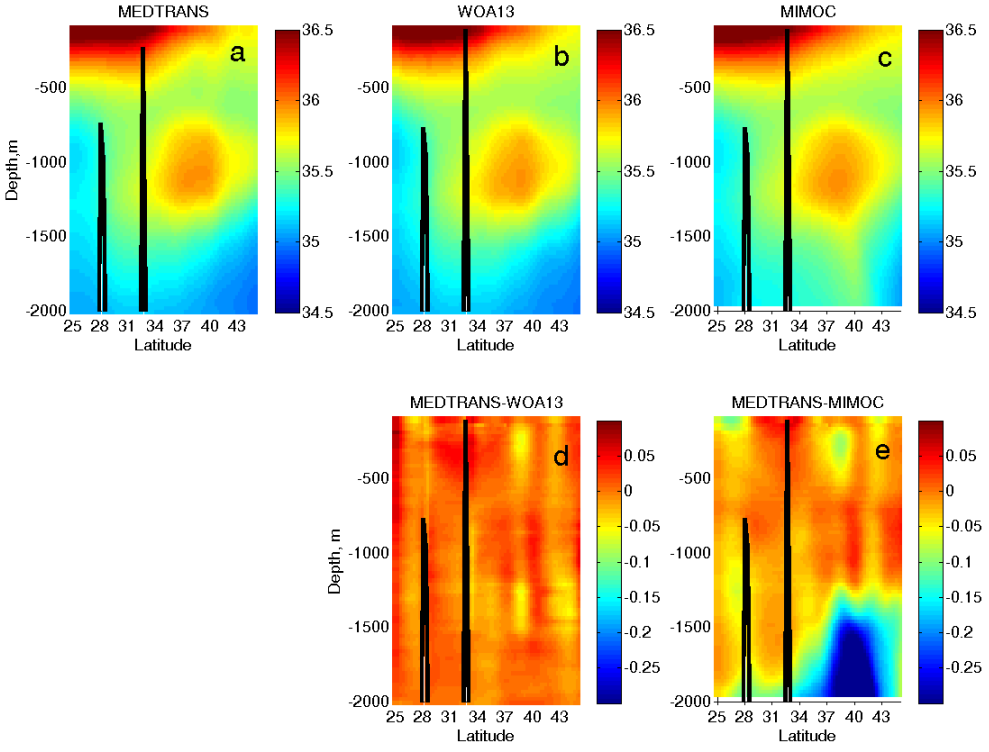

Figure 6. Meridional sections of salinity along 17° W: **(a)** MEDTRANS, **(b)** WOA13, **(c)** MIMOC, **(d)** MEDTRANS minus WOA13, and **(e)** MEDTRANS minus MIMOC.

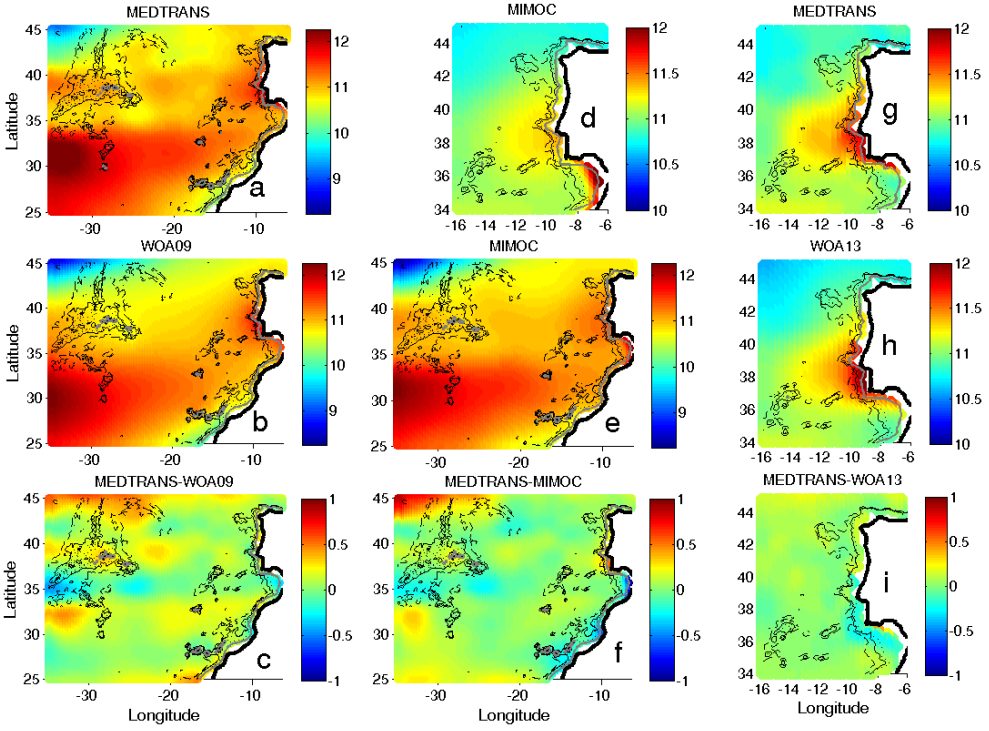

Figure 7. Temperature at 600 m. All regions: **(a)** MEDTRANS, **(b)** WOA09, **(c)** MEDTRANS minus WOA09, **(e)** MIMOC, and **(f)** MEDTRANS minus MIMOC. Zoom to the Iberian Peninsula: **(d)** MIMOC, **(g)** MEDTRANS, **(h)** WOA13, and **(i)** MEDTRANS minus WOA13.

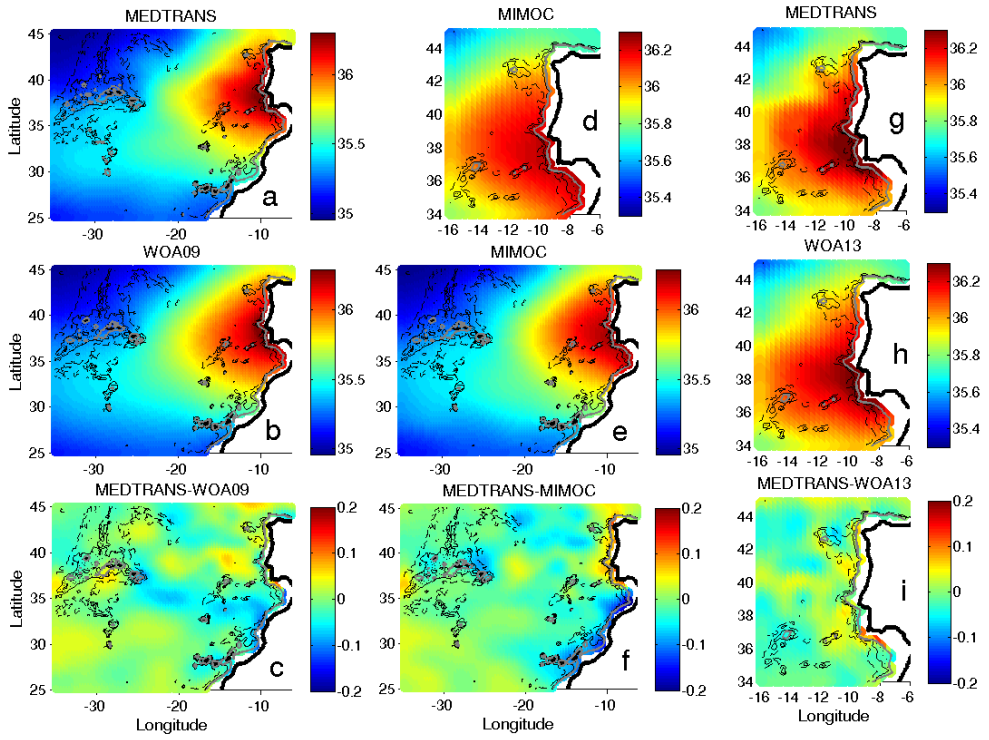

Figure 8. Salinity at 1200 m. All regions: **(a)** MEDTRANS, **(b)** WOA09, **(c)** MEDTRANS minus WOA09, **(e)** MIMOC, and **(f)** MEDTRANS minus MIMOC. Zoom to the Iberian Peninsula: **(d)** MIMOC, **(g)** MEDTRANS, **(h)** WOA13, and **(i)** MEDTRANS minus WOA13.

detail in MEDTRANS. The MEDTRANS climatology also makes noticeable a second, weaker local salinity maximum, which extends to the Azores plateau from the south at 28–30° W and 35–36° N (Fig. 8a). Compared to other climatologies, the MEDTRANS climatology reproduces much more detail of the two intrusions of Subarctic Intermediate Water (SIAW) and the LSW (Arhan, 1990; Bower et al., 2002): along the northeastern part of the Azores plateau (37–40° N, 24–28° W) and along the Kings rise/trough (42–45° N and 21–25° W) (Fig. 8a–c and e–f). At the Iberian Peninsula, an important additional detail of MEDTRANS is the MUC separation into two branches at the southern slope of the Galicia Bank (Fig. 8g, h and f). This detail is missing in other climatologies, including WOA13.

At 1700 m (Fig. 9a–c), MEDTRANS presents more detail in the structure of the deeper portion of the MW tongue compared to WOA09, but is not intrinsically different to WOA13 (Fig. 9g–i). At the same time, the MIMOC climatology shows a strange finger-like MW salinity pattern between 35 and 43° N (Fig. 9e–f). Salinity profiles of the MIMOC climatology (Fig. 9d, profile 3) show unrealistically deep MW influence, which cannot be identified in the original data distributions at those deep levels (Figs. 1b and 9d). The same feature is observed in temperature (not shown). This is an artefact of the MIMOC climatology.

Spatial distributions for a layer mean N^2 are generally similar for all three data sets (Fig. 10). For the same latitude, N^2 is a proxy for potential vorticity, and its distribution can be used for detection of water masses. The N^2 distribution in the upper main thermocline (Fig. 10a–c) displays lower values in the northeastern corner, corresponding to the areas of generation and spreading of the polar fraction of the East Atlantic Central Water (Pollard et al., 1996; Paillet and Mercier, 1997). At intermediate water levels (Fig. 10d–f), a N^2 minimum is situated at the Iberian Peninsula and is a sign of the MW. Another minimum, extending along the African coast from 25 to 33° N, corresponds to the northward penetration of the AAIW (Louarn and Morin, 2011). At deep water levels (Fig. 10g–h), the N^2 minimum in the northwestern corner of the region, extending southeast along the eastern slope of the MAR, is due to the southward spreading of the LSW (Bower et al., 2002). At those levels, MIMOC again shows artificial structures in N^2 compared to other climatologies. In MIMOC, the anomalously low N^2 values result from anomalously weak vertical variations of temperature and salinity at those deep levels (Fig. 9d, point 3).

Figure 11 shows geostrophic currents referred to the 1900 m level, computed from the MEDTRANS, WOA13 and MIMOC annual climatologies. Currents from the WOA09 climatology are not presented since they are over-smoothed, even compared to the MIMOC climatology. A depth of 1900 m is chosen as the reference level, since the adjacent layers present the smallest variations of isopycnal depth over the study region. The reference-level currents in the study re-

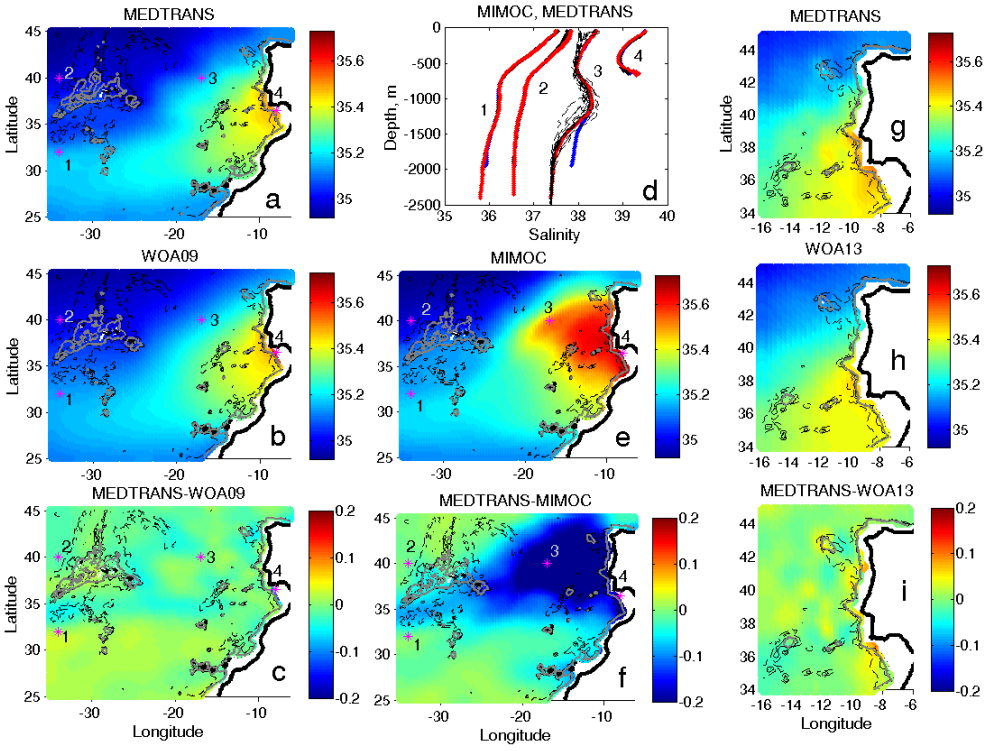

Figure 9. Salinity at 1700 m; **(a)** and **(g)** MEDTRANS, **(b)** WOA09, **(c)** MEDTRANS minus WOA09, **(e)** MIMOC, **(f)** MEDTRANS minus MIMOC, **(h)** WOA13, and **(i)** MEDTRANS minus WOA13. Plate **(d)** presents vertical profiles of MEDTRANS (red) and MIMOC (blue) at points 1 (32° N, 34° W), 2 (40° N, 34° W), 3 (40° N, 17° W), and 4 (37° N, 8° W). WOA13 profiles (black) are not seen since they are nearly identical to MEDTRANS profiles for points 1–3 and to the MIMOC profile for point 4. Dashed lines over climatic profile 3 are the observed CTD casts within a 10 km distance from this point.

gion, derived from Argo floats, are of the order of 1 cm s^{-1} (Calheiros and Bashmachnikov, personal communication), which can be taken as the measure of the computational error of the upper ocean current velocities.

Figure 11a shows the currents at 100 m depth, while Fig. 11b displays the mean currents derived from AVISO altimetry (AVISO). The AVISO currents are averaged from 1992 to 2012. The latest version of the mean dynamic topography CNES-CLS09_v1.1 (Rio et al., 2011) is used for computation of the current velocities.

The MEDTRANS currents are similar in structure and intensity to those obtained from altimetry. Thus, the velocity of the AzC jet in the MEDTRANS climatology and in AVISO varies from 10–12 cm s^{-1} south of the Azores to 6–8 cm s^{-1} to the east, although the flow in MEDTRANS is a bit too wide. The MEDTRANS climatology also shows intensification of the flows in the northern and southern parts of the Gulf of Cadiz, as well as south of the Canary Islands. It also reproduces an anticyclonic re-circulation south of the AzC at 31–35° W and a cyclonic circulation in the Gulf of Cadiz at 9–10° W, as well as the merging of the two branches of the SNAC west of the MAR: one enters the study region at 40° N and the other at 44° N.

The comparison with the MIMOC climatology clearly shows advantages of MEDTRANS in providing a detailed representation of the circulation patterns (Fig. 11d). There are more similarities to the geostrophic currents estimated from WOA13 (Fig. 11c). However, the latter gives less evidence of the AzC meandering and periodic along-path intensification that is observed in AVISO and MEDTRANS. In addition, the WOA13 climatology does not reproduce the cyclonic gyre in the Gulf of Cadiz (Fig. 11a–b) as well as the MUC (Fig. 11e–f) along the northern slope of the Gorringe Bank and the southern slope of the Galicia Bank (Iorga and Losier, 1999).

Figure 11a shows that the AzC decelerates as it turns north in quasi-stationary meanders and accelerates as it turns south. This feature is also apparent in AVISO results (Fig. 11b), but is absent in WOA13 results (Fig. 11c). The strongest stationary meander is situated at 21–22° W (in AVISO data – at 23° W) and the second one at 16–17° W (the same in AVISO data).

The observed deceleration of the AzC in the meanders, as the jet turns north, is accompanied by widening of the jet and an outflow from the jet to the north at 22 and 17° W (Fig. 11a). The merging of the streamlines and the acceleration of the AzC, as the jet turns south, is accompanied by

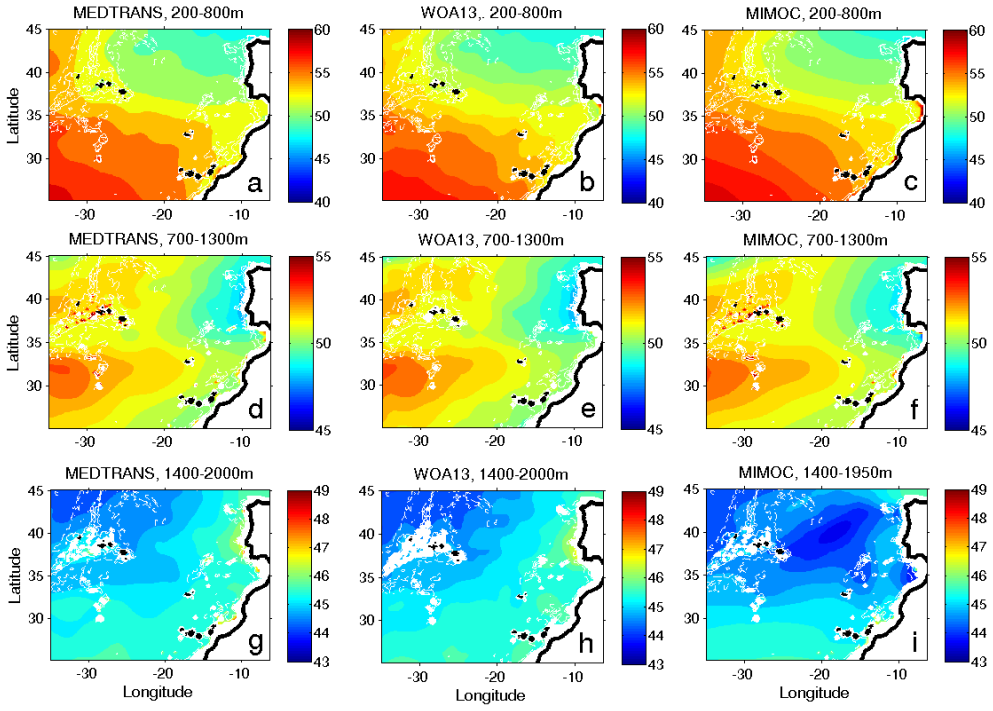

Figure 10. N^2: **(a–c)** average from 200 to 800 m, **(d–f)** average from 700 to 1300 m, and **(g–i)** average from 1400 to 2000 m, for MEDTRANS (the first column), WOA13 (the second column) and MIMOC (the third column).

inflows into the AzC from the north at 20, 16 and 13° W. The southward meandering of the AzC ends with the branches to the south at 17 and 12° W (there are also outflows at 31–32 and 27–28° W). Therefore, quasi-stationary meanders in the AzC form semi-closed water circulations to the north and to the south of the jet. Those features are missing in WOA13 or MIMOC climatologies. The abovementioned inflows/outflows to/from the AzC jet, as it meanders, may be a result of the accumulated effect of cross-jet migrations of particles subjected to inertial forces (Cushman-Rosin, 2010). At the same time, estimated local inertial effects are small, within 1 % of the computed geostrophic current velocities, and do not affect the presented flow structure.

The symmetry of the water inflows/outflows in a meandering current, predicted by the theory, is broken in nature by the vorticity constraint. The anticyclonic vorticity pumped into the ocean by the wind demands that the overall flow go south (the Sverdrup flux). Therefore, the currents are more readily merging with the AzC from the north and leaving it to the south than vice versa.

3.2 Seasonal variability in the MEDTRANS climatology

The gridding procedure is repeated for the warm (May–October) and cold (November–April) seasons. The data are nearly equally distributed over the year: the cold season contains 25 000 profiles, while the warm one contains 29 000 profiles. The mean window size containing at least 30 points increases by 30–50 % (depending on the G level and the season), as compared to that derived from the complete data set. Therefore, to keep the distributions smooth enough, we increase the Barnes gridding radius by 50 % relative to the annual climatic mean (Sect. 3.1). Thus, for G less than or equal to 27.96 kg m^{-3} (the upper 1900 m layer), R is taken 150 km near the Iberian coast and 300 km in the western part of the region. Its spatial variation is identical to the one presented in Fig. 4a.

Figure 12 presents salinity distributions during the cold (Fig. 12a, d and g) and warm (Fig. 12b, e and h) seasons at selected water levels, as well as the respective differences between the seasons (Fig. 12c, f and j). In the upper thermocline (Fig. 12a–c), the cold season is characterized by a hump-like feature between 15 and 25° W at around 35° N, while in summer, the isohalines are closer to zonal. The effect is clearly seen in the seasonal change of the intensity of the AzC meander in this region (Fig. 13a–b). This seasonal pattern was first described by Käse and Siedler (1982). The feature is not seen in WOA13 seasonal climatologies of salinity and geostrophic currents, but is well reproduced in the corresponding MIMOC seasonal climatologies (not shown). More strict zonal extension of the flows in summer can be explained by the seasonal difference in the wind-induced ocean vorticity. In summer, seasonal weakening of the wind stress curl by 50 % (Dee et al., 2011), except for the trade winds in the Canary upwelling area, leads to a reduction in the

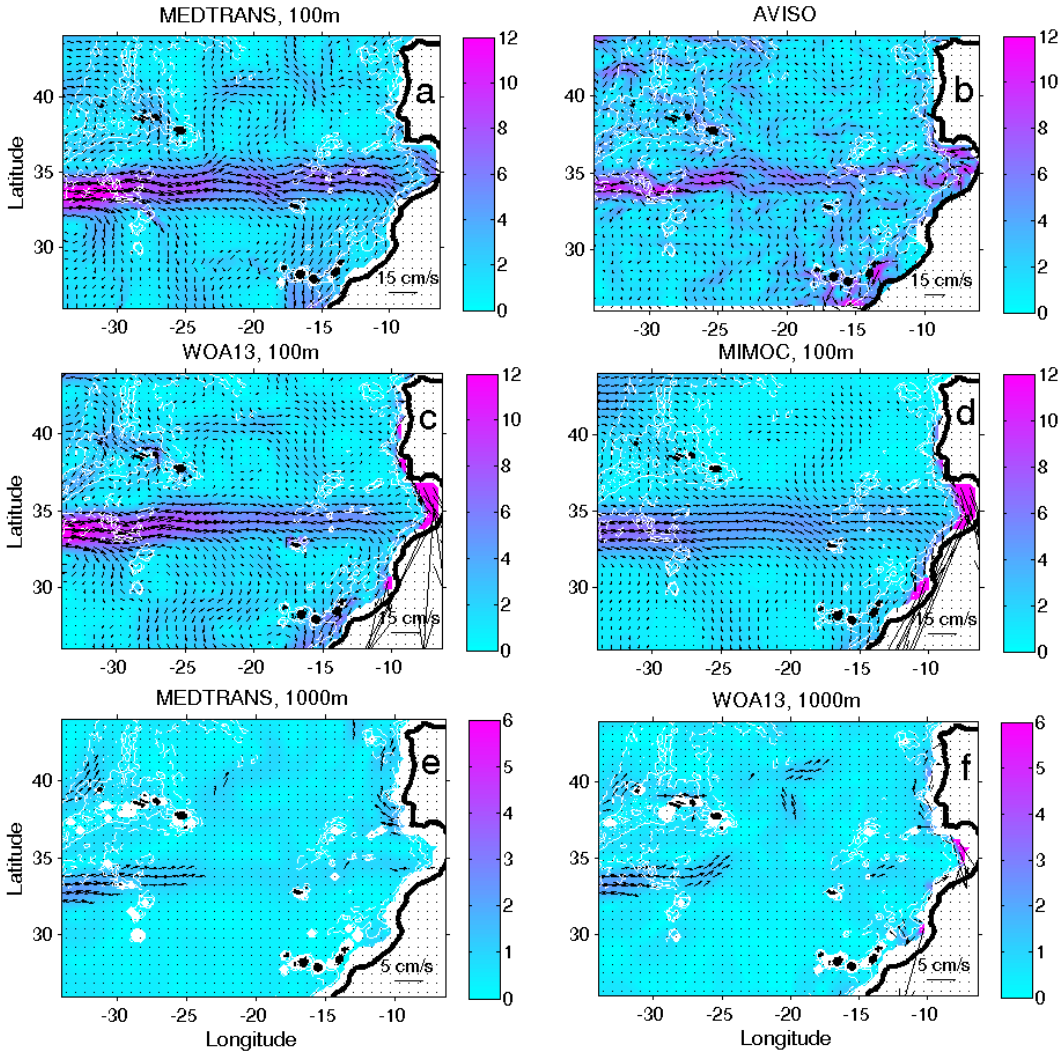

Figure 11. Velocity of geostrophic currents ($cm\,s^{-1}$) at 100 m referenced to 1900 m, derived from **(a)** MEDTRANS, **(c)** WOA13 and **(d)** MIMOC. AVISO surface currents, averaged between 1992 and 2012, are presented in **(b)**. Velocity of geostrophic currents at 1000 m referenced to 1900 m ($cm\,s^{-1}$), derived from **(e)** MEDTRANS and **(f)** WOA13. Velocity vectors are overlaid. For reference, 2000 m and 3000 m depth contours are shown in white.

meridional Sverdrup transport. Therefore, Eq. (1) is satisfied better than during the cold season, and currents tend to become more closely aligned with the contours of constant f (when their directions are not conditioned by steep topographic slopes).

The seasonal variation also influences the path of the AzC. In Sect. 3.1 the meander at around 21–22° W was noted. Figures 12a–b and 13a–b, as well as seasonal means of AVISO altimetry currents (not shown), give evidence that the meander is mostly pronounced during winter and nearly disappears in summer. Only this section of the AzC presents a seasonal variation of its meridional position (see also Siedler and Finke, 1993). This removes inconsistency between the reported 2° northward shift of the front of the AzC in winter, obtained from a coarse-resolution study by Stramma and Siedler (1988), and a recently demonstrated stability (within 0.25° limit) of the AzC axis, integrated over the full length of the current (Lázaro et al., 2013).

Along the western coast of the Iberian Peninsula and the northwestern coast of Africa (from the Canary Islands to the Gulf of Cadiz), water at 200 m depth is fresher (Fig. 12c) and colder (not shown) during the warm season, when stronger southward winds along the coast form/intensify the coastal Portugal and Canary upwellings (Navarro-Perez and Barton, 2001; Fraile-Nuez et al., 2010). This feature is also well reproduced by both the WOA13 and the MIMOC seasonal climatologies. The resulting stronger uplift of the isopycnals along the coasts is apparent in zonal sections of the MEDTRANS climatology (not shown). For example, along the northwestern African coast, the seasonal variation of the

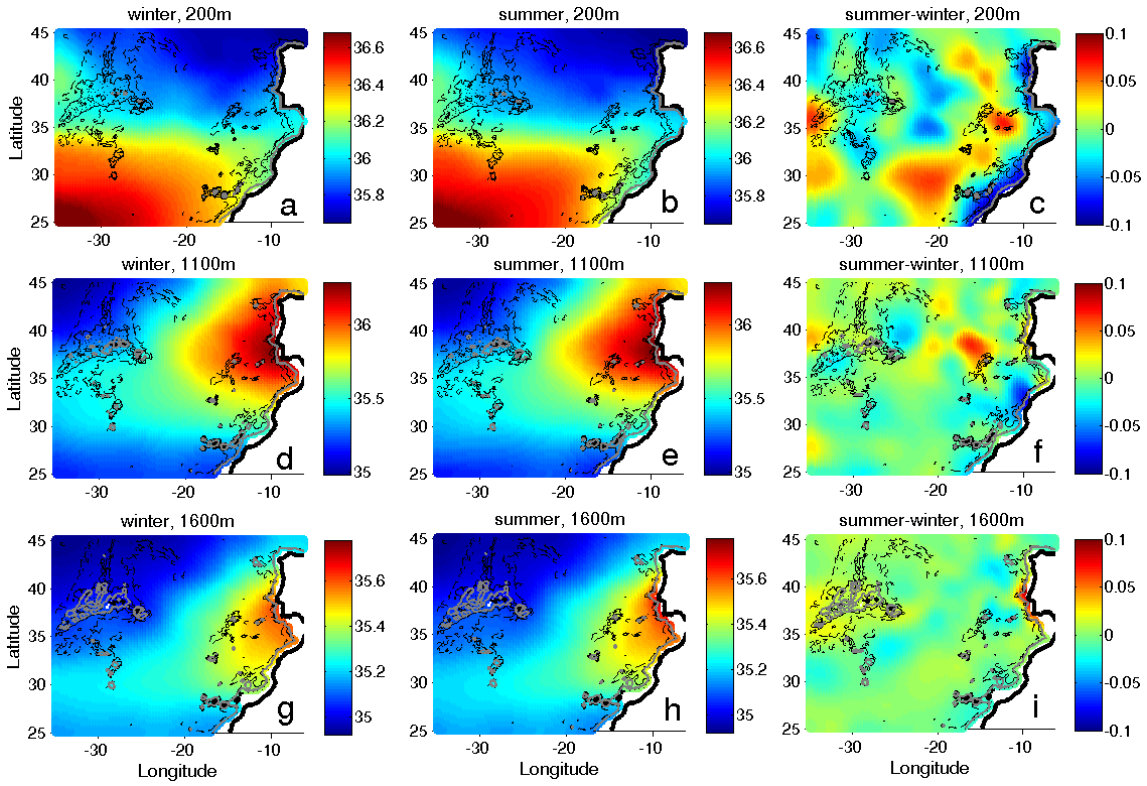

Figure 12. Salinity at **(a, b)** 200 m, **(d, e)** 1100 m and **(g, h)** 1600 m: **(a)**, **(d)** and **(g)** – winter; **(b)**, **(e)** and **(h)** – summer; **(c)**, **(f)** and **(i)** – difference between the summer and winter climatologies.

maximum coastal uplift of isopycnals in the upper 200 m layer changes from a few meters at 34° N (Casablanca) to 25 m between 28° N (Cape Jubi) and 33° N, and to more than 50 m at 26° N (Cape Bojador). The seasonality in the uplift quickly decreases in amplitude to a few meters at 250–350 m depth between 28 and 33° N, but is observed down to 600 m at 26° N.

In the intermediate water levels, the spreading of the MW shows little seasonality (Fig. 12d–f). However, during the warm season, the MW salinity tongue at the level of the lower MW core (1000–1300 m) is stretched farther west and is more squeezed in the meridional direction. In the WOA13 and MIMOC seasonal climatologies, those seasonal variations are less pronounced (not shown). The observed seasonality is in phase with that in the upper ocean and may equally be a result of a change in the intermediate layer circulation as a response to the seasonal intensification in the wind forcing described above. Northeast of the Canary Islands, along the African coast, the farther northward penetration of the AAIW during the spring–summer seasons (Machin and Pelegri, 2009) is also apparent in MEDTRANS – a negative salinity anomaly in the warm–cold season difference (Fig. 12f). The patterns of geostrophic circulation at intermediate levels are presented in Fig. 13c–d. The current patterns mostly show the same tendency as in the upper thermocline: they are more extended in the zonal direction during summer. In particular, we note a summer intensification of the zonal flow north of the Gorringe Bank. Though the weak currents at those depths may be influenced by non-zero flows at the reference level (of around 1 cm s^{-1}), the detected seasonality in the current patterns goes parallel to the corresponding seasonal variation of the zonal extension of temperature–salinity patterns. (Fig. 12d–f). Some very weak traces of those seasonal patterns can be detected in MIMOC seasonal climatologies, while the WOA13 seasonal climatology does not show any clear difference in circulation patterns at those depths (not shown).

Salinity (and temperature) distributions at 1600 m depth (Fig. 12g–i) suggest that seasonality at those depths is very weak, except for the deeper part of the Iberian continental margin.

Figure 14 presents the depth and intensity of the near-slope salinity maxima along the Iberian coast, i.e. the characteristics of the lower core of the MUC. The results show that, on average, during the warm season the MUC is more saline by 0.02–0.04, and the computed density at the maximum salinity level is larger by 0.01 kg m^{-3}. This may result from a more saline summer outflow from the Mediterranean Sea (Sparnocchia et al., 1994), as well as from higher salinity of

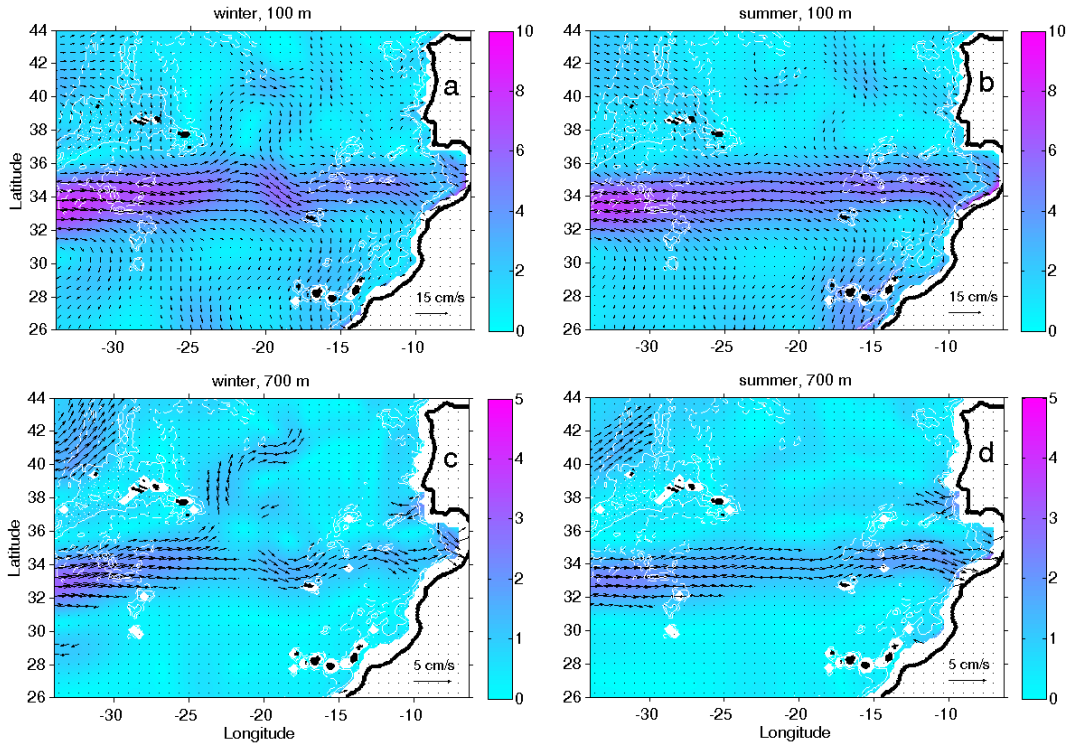

Figure 13. Velocity of geostrophic currents ($cm\,s^{-1}$) at the 100 m and 700 m levels, referenced to 1900 m: **(a)** 100 m winter, **(b)** 100 m summer, **(c)** 700 m winter, **(d)** 700 m summer. Velocity vectors are overlaid.

the North Atlantic Central Water (NACW) entrained in the MUC in the Gulf of Cadiz.

The apparent increase in the MEDTRANS gridded salinity along the southern margin of the Iberian Peninsula (Fig. 14, 7–8.5° W) results from over-smoothing of the MUC characteristics in the immediate vicinity of the Strait of Gibraltar. In this area the MUC is only 20–50 km wide (Baringer and Price, 1997) and the 70 km gridding window produces its artificial mixture with the fresher and colder NACW. However, the depth of the core is correctly represented in the climatology. Interesting features are sudden changes in the depth of the lower MUC at some topographically relevant locations, its depth otherwise being quite stable. Thus, the depth of the MUC increases by 25 m across the Portimão canyon (8.3 to 8.7° W), then decreases by around 100 m at Cape St. Vincent (37° N, winter) or 1° north of it (summer), at Aveiro canyon (40.5-41° N) and at Cape Finisterre (43° N). These results are in accordance with previous estimates of along-slope variations of the depth of the MW salinity maximum (Daniault et al., 1994; Bower et al., 2002).

Another feature observed in the climatology is the change in thickness of the salty MW along the Iberian continental slope, represented as vertical segments in Fig. 14. At each section perpendicular to the isobaths, the thickness is computed as the maximum depth difference between isohalines corresponding to 99 % of the maximal salinity of the section (the same results are obtained using a fixed value of 36.9 for the limiting isohaline). The thickness of the flow increases up to 38–39° N (southern flank of the Estremadura Promontory) and then starts decreasing. The MW outflow from the Strait of Gibraltar entrains 3/4 of the volume while passing the first 20–40 km along the northern slope of the Gulf of Cadiz at depths of 250–500 m. Farther on, entrainment into the MW continues, but to a lesser degree (Baringer and Price, 1999). The observed tendencies in the MW core thickness near the Iberian Peninsula suggest that the Estremadura Promontory is a boundary between the MUC dominated by entrainment of the surrounding water into it and the MUC dominated by dispersion of the water from it.

4 Conclusions

The MEDTRANS climatology is based on the Barnes optimum interpolation procedure on 53 neutral density surfaces. Due to lower along-surface gradients of temperature and salinity, as compared to the isobaric surfaces, the isoneutral gridding provides a better representation of sharp thermal and haline fronts for the same gridding radius. This is further proven when computing geostrophic current velocities in comparison with the existing high-resolution isobaric data sets (WOA09 and WOA13). The hydrological data used for compiling the climatology have undergone several filtering procedures, including filtering on neutral density surfaces.

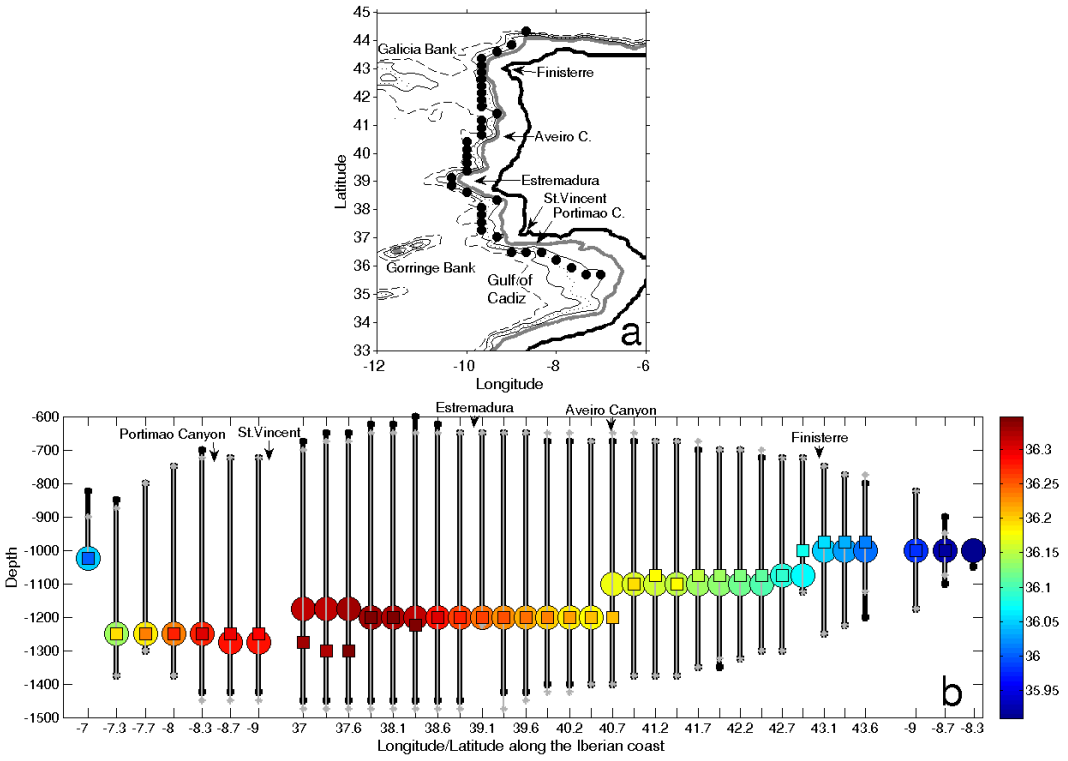

Figure 14. (a) Positions of the axis of the lower MW core derived from the MEDTRANS data set (black dots), overlaid on bathymetry of the Iberian–Canary basins. **(b)** Seasonal variations of the depth and salinity of the lower MW core along the Iberian slope in the cold season (disks) and warm season (squares). The vertical segments represent the maximum depth limits of $S \geq 0.99 \times S\mathrm{max}$ at the section.

Reducing eddy-related and instrumental noise, the filtering allows sufficient smoothness of the final thermohaline fields at the enhanced spatial resolution. The gridding window radius decreases towards the northeast, allowing the best use of the large number of data near the Iberian Peninsula. In particular, this leads to a better representation of thermohaline fronts of the Iberian upwelling and the MUC. The final climatological maps of temperature and salinity distributions are further vertically re-gridded to the isobaric levels to have a 25 m depth interval with around 30 km horizontal resolution.

The MEDTRANS gridding procedure can be regarded as a development of some of the ideas used for obtaining the MIMOC data set (Schmidtko et al., 2013). However, there are a few important differences, which allow the MEDTRANS data set to show several advantages compared to MIMOC. Based on vorticity considerations, the topographic influence on the dominant along-slope direction of water mass propagation for steep slopes is taken into account through the shape of the gridding function. The degree to which the gridding weights are aligned with the isobaths along steep slopes depends on the ratio of topographic to planetary β-effects. Limitations on the maximum possible stretching of the gridding window along isobaths increases the reliability of the results along very steep slopes, where otherwise the weight function elongates in a very thin line with only a few observational points inside. The baroclinic decrease in the topographic effect with the distance between the gridding level and the ocean bottom is taken into account: the maximum distance of the topographic influence is proportional to the N/f ratio. In the study region, the ratio is taken constant, as observed. For larger regions, a decrease in the ratio towards the equatorial region and its strong increase towards the polar waters should be accounted for. In particular, in polar regions the currents are nearly barotropic and the transition occur in a jump when crossing the subpolar and polar fronts (Cuny et al., 2002; Losch and Schröter, 2004).

We did not stretch the weight function in the zonal direction whenever the influence of the bathymetry can be neglected. This is justified over most of the ocean, where the wind stress curl forces a significant meridional component of the flow. At the same time, the zonal extension may give advantages near the Equator, where, due to the strong meridional gradient of the Coriolis parameter, the zonal extension of the flow is well pronounced (Schmidtko et al., 2013).

The MEDTRANS climatology gives more details of the distribution of water characteristics in the upper 2000 m layer over the subtropical northeastern Atlantic, compared to other climatologies. As in other climatologies, the meandering, together with the seasonal and interannual variations of the

current position, enlarges the width of the jets in the climatological fields compared with the instantaneous characteristics of the currents. At the same time, the geostrophic currents, derived from the MEDTRANS climatology, reveal several features not reproduced by the existing climatologies but in close correspondence to independent observations (e.g. Lozier et al., 1995; New et al., 2001) and theory (Cushman-Rosin, 2010): (i) periodic intensification of the AzC as it turns south in quasistationary meanders; (ii) inflows and outflows in the AzC meanders; (iii) recirculation of the AzC west of the Cruiser–Great Meteor seamounts; and (iv) a cyclonic beta gyre in the Gulf of Cadiz. At 1000 m depth, the geostrophic currents referring to the 1900 m level, derived from the MEDTRANS data set, show two veins of the MUC along the western slope of the Iberian Peninsula: one travels along the slope, while the other separates from the slope around the Gorringe Bank and then merges with the other vein, south of the Galicia Bank. Here the MUC splits again into a vein along the continental slope directed north and along the southwestern slope of the Galicia Bank directed northwest. Those veins have been previously noted (Iorga and Losier, 1999), but do not appear in WOA13 or MIMOC climatologies.

The seasonality of the MW manifests itself in stronger zonal extension of the patterns during the warm season. This may be related to the decrease in the wind stress curl, and the consequent decrease in the meridional Sverdrup transport. Near the Iberian slope, the lower core of the MUC is noted to be more saline and denser during the warm season, as compared to the cold one. The MUC is not correctly represented in alternative climatologies, including WOA13.

The gridded temperature–salinity fields are available at the website of the Center of Oceanography of the University of Lisbon (http://co.fc.ul.pt/en/data).

Appendix A

To obtain an indication of the value of R, which filters the remnant eddy noise, decorrelation spatial scales of temperature–salinity data are computed for each data point. Only the points which have at least 10 neighbouring observations within a 200 km radius and a 30-day period are used (Fig. A1). The decorrelation scales are estimated in three ways: as the point of zero crossing of a cosinusoidal fit to the autocorrelation function, as the integral of the normalized autocorrelation function, from zero to the first zero crossing, and as the integral of the square of the normalized autocorrelation function over its definition range (Stammer, 1997).

The histogram of the decorrelation scales, a proxy for eddy radii (Fig. A1 in the Appendix), shows that the scales have two modes: at 10–20 km and around 30 km, and ranging from 10 to 100 km. The latter mode is close to the Rossby radius of deformation in the study region (Emery et al., 1984). The distribution of the decorrelation radii does not show any significant variation across the study region, neither with latitude nor with the proximity to steep topography. The latter values compare well with the previous studies in the region. In situ observations suggest eddy radii between 40 and 100 km in the area of the AzC (Gould, 1985; Pollard and Pu, 1985; Pingree and Sinha, 1998; Alves and Verdiere, 1999; Alves et al., 2002; Pingree, 2002; Mourino et al., 2003) and between 10 and 60 km in the northern part of the study region (Arhan and Colin de Verdiere, 1985; Mercier and Colin de Verdiere, 1985; Shoosmith et al., 2005), as well as in the upwelling area near the Iberian Peninsula (Pingree and LeCann, 1992; Oliveira et al., 2004). Derived from the satellite altimetry, the characteristic eddy scales in the study region are estimated to be 40–80 km (Le Traon et al., 1990) and 60–100 km (Stammer, 1997; Jacobs et al., 2001; Chelton et al., 2011). The overall larger radii derived from the AVISO altimetry are biased by the cut-off length of 40–50 km, below which eddies cannot be detected with the gridded altimetry data.

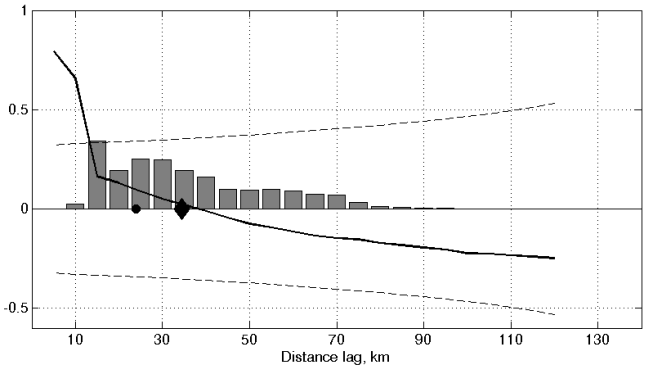

Figure A1. Regional-mean decorrelation scales (radii): the black curve is the mean autocorrelation function, and the black diamond is the mean of the decorrelation scales, while the black disk is the decorrelation scale computed from the mean autocorrelation function (black curve). Dash lines mark the level of significance of the mean autocorrelation function. Bars present the normalized histogram of regional-mean eddy radii.

Acknowledgements. The authors acknowledge the MEDTRANS scientific project (PTDC/MAR/117265/2010), sponsored by the Portuguese Foundation for Science and Technology (FCT) and the MARE – Marine and Environmental Sciences Centre of Oceanography of the University of Lisbon (CO-Pest-OE/MAR/UI0199/2011). I. Bashmachnikov also acknowledges contract C2008-UL-CO-3 of Ciência 2008 between the Foundation for Science and Technology (FCT) and the University of Lisbon (UL).

Edited by: D. Stevens

References

Alves, M. L. G. R. and de Verdière, A. C.: Instability dynamics of a subtropical jet and applications to the Azores current system: eddy-driven mean flow, J. Phys. Oceanogr., 29, 837–864, 1999.

Alves, M. L. G. R., Gaillard, F., Sparrow, M., Knoll, M., and Giraud, S.: Circulation patterns and transport of the Azores front-current system, Deep-Sea Res. II, 49, 3983–4002, 2002.

Ambar, I.: A shallow core of Mediterranean water off western Portugal, Deep-Sea Res. A, 30, 677–680, 1983.

Ambar, I., Serra, N., Neves, F., and Ferreira, T.: Observations of the Mediterranean Undercurrent and eddies in the Gulf of Cadiz during 2001, J. Marine Syst., 71, 195–220, 2008.

Arhan, M.: The North Atlantic Current and Subarctic Intermediate Water, J. Mar. Res., 48, 109–144, 1990.

Arhan, M. and Colin de Verdiere, A.: Dynamics of eddy motions in the eastern North Atlantic, J. Phys. Oceanogr., 15, 153–170, 1985.

Baringer, M. N. and Price, J. F.: Mixing and Spreading of the Mediterranean Outflow, J. Phys. Oceanogr., 27, 1654–1677, 1997.

Baringer M. N. and Price, J. F.: A review of the physical oceanography of the Mediterranean outflow, Mar. Geol., 155, 63–82, 1999.

Barnes, S. L.: A Technique for Maximizing Details in Numerical Weather Map Analysis, J. Appl. Meteorol., 3, 396–409, 1964.

Bower, A. S., Le Cann, H., Rossby, T., Zenk, W., Gould, J., Speer, K., Richardson, P. L., Prater, M. D., and Zhang, H. M.: Directly measured mid-depth circulation in the North Atlantic Ocean, Nature, 419, 603–607, 2002.

Chelton, D. B., Schlax, M. G., and Samelson, R. M.: Global observations of nonlinear mesoscale eddies, Prog. Oceanogr., 91, 167–216, 2011.

Cipollini, P., Cromwell, D., Jones, M. S., Quartly, G. D., and Challenor, P. G.: Concurrent altimeter and infrared observations of Rossby wave propagation near 34^{o}N in the Northeast Atlantic, Geophys. Res. Lett., 24, 889–892, 1997.

Comas-Rodríguez, I., Hernández-Guerra, A., Fraile-Nuez, E., Martínez-Marrero, A., Benítez-Barrios, V. M., Pérez-Hernández, M. D., and Vélez-Belchí, P.: The Azores Current System from a meridional section at 24.5° W, J. Geophys. Res., 116, C09021, doi:10.1029/2011JC007129, 2011.

Cuny, J., Rhines, P. B., Niiler, P. P., and Bacon, S.: Labrador Sea boundary currents and the fate of the Irminger Sea Water, J. Phys. Oceanogr., 32, 627–647, 2002.

Cushman-Roisin, B.: Environmental Fluid Mechanics, John Wiley & Sons, NY, 400, 2010.

Daniault, N., Mazé, J. P., and Arhan, M.: Circulation and mixing of Mediterranean Water west of the Iberian Peninsula, Deep-Sea Res. I, 41, 1685–1714, 1994.

Dee, D. P., Uppala, S. M., Simmons, A. J., Berrisford, P., Poli, P., Kobayashi, S., Andrae, U., Balmaseda, M. A., Balsamo, G., Bauer, P., Bechtold, P., Beljaars, A. C. M., van de Berg, L., Bidlot, J., Bormann, N., Delsol, C., Dragani, R., Fuentes, M., Geer, A. J., Haimberger, L., Healy, S. B., Hersbach, H., Hólm, E. V., Isaksen, L., Kållberg, P., Köhler, M., Matricardi, M., McNally, A. P., Monge-Sanz, B. M., Morcrette, J. J., Park, B. K., Peubey, C., de Rosnay, P., Tavolato, C., Thépaut, J. N., and Vitart, F.: The ERA-Interim reanalysis: configuration and performance of the data assimilation system, Q. J. R. Meteorol. Soc., 137, 553–597, 2011.

Emery, W. J., Lee, W. G. and Magaard, L.: Geographic and Seasonal Distributions of Brunt–Väisälä Frequency and Rossby Radii in the North Pacific and North Atlantic, J. Phys. Oceanogr., 14, 294–317, 1984.

Emery, W. J. and Thomson, R. E.: Data analysis methods in physical oceanography, Pergamon, UK, 634 pp., 1997.

Fraile-Nuez, E., Machín, F., Vélez-Belchí, P., López-Laatzen, F., Borges, R., Benítez-Barrios, V., and Hernández-Guerra, A.: Nine years of mass transport data in the eastern boundary of the North Atlantic Subtropical Gyre, J. Geophys. Res., 115, C09009, doi:10.1029/2010JC006161, 2010.

Gould, W. J.: Physical oceanography of the Azores front, Prog. Oceanogr., 14, 167–190, 1985.

Gouretski, V. V. and Koltermann, K. P.: Berichte des Bundesamtes für Seeschifffahrt und Hydrographie Nr. 35, 2004.

Harvey, J.: θ-S relationships and water masses in the eastern North Atlantic, Deep-Sea Res., 29, 1021–1033, 1982.

Jacobs, G. A., Barron, C. N., and Rhodes, R. C.: Mesoscale characteristics, J. Geophys. Res., 106, 19581–19595, 2001.

Jackett, D. R. and McDougall, T. J.: A Neutral Density Variable for the World's Oceans, J. Phys. Oceanogr., 27, 237–263, 1997.

Jia, Y.: Formation of an Azores Current Due to Mediterranean Overflow in a Modeling Study of the North Atlantic, J. Phys. Oceanogr., 30, 2342–2358, 2000.

Iorga, M. C. and Lozier, M. S.: Signature of the Mediterranean outflow from a North Atlantic climatology: 1. Salinity and density fields, J. Geophys. Res., 104, 25985–26009, 1999.

Kantha, L. H. and Clayson, C. A.: Numerical models of oceans and oceanic processes. International Geophysics series v.66, Acad. Press, San Diego, 887 pp., 2000.

Kase, R. H. and Siedler, G.: Meandering of the subtropical front south-east of the Azores, Nature, 300, 245–246, 1982.

Klein, B. and Siedler, G.: On the origin of the Azores current, J. Geophys. Res., 94, 6159–6168, 1989.

Lázaro, C., Juliano, M. F., and Fernandes, M. J.: Semi-automatic determination of the Azores Current axis using satellite altimetry: Application to the study of the current variability during 1995–2006, Adv. Space Res., 51, 2155–2170, 2013.

Le Traon, P. Y., Rouquet, M. C., and Boissier, C.: Spatial scales of mesoscale variability in the North Atlantic as deduced from Geosat data, J. Geophys. Res., 95, 20267–20285, 1990.

Levitus, S., Antonov, J., and Boyer, T.: Global ocean heat content 1955–2007 in light of recently revealed instrumentation problems, Geophys. Res. Lett., 36, L07608, doi:10.1029/2008GL037155, 2008.

Losch, M. and Schröter, J.: Estimating the circulation from hydrography and satellite altimetry in the Southern Ocean: limitations imposed by the current geoid models, Deep-Sea Res. Pt. I, 51, 1131–1143, 2004.

Louarn, E. and Morin, P.: Antarctic Intermediate Water influence on Mediterranean Sea Water outflow, Deep-Sea Res. Pt. I, 58, 932–942, 2011.

Lozier, M. S., McCartney, M. S., and Owens, W. B.: Anomalous anomalies in averaged hydrographic data, J. Phys. Oceanogr., 24, 2624–2638, 1994.

Lozier, M. S., Owens, W. B., and Curry, R. G.: The climatology of the North Atlantic, Prog. Oceanogr., 36, 1–44, 1995.

Machín, F. and Pelegrí, J. L.: Northward Penetration of Antarctic Intermediate Water off Northwest Africa, J. Phys. Oceanogr., 39, 512–535, 2009.

Martins, C. S., Hamann, M., and Fuiza A. F. G.: Surface circulation in the eastern North Atlantic from drifters and altimetry, J. Geophys. Res., 107, 3217, doi:10.1029/2000JC000345, 2002.

Maximenko, N. A., Melnichenko, O. V., Niiler, P. P., and Sasaki, H.: Stationary mesoscale jet-like features in the ocean, Geophys. Res. Lett., 35, L08603, doi:10.1029/2008GL033267, 2008.

McDougall, T. J.: Neutral density surfaces, J. Phys. Oceanogr., 17, 1950–1964, 1987.

Melet, A., Nikurashin, M., Muller, C., Falahat, S., Nycander, J., Timko, P. G., Arbic, B. K. and Goff., J. A.: Internal tide generation by abyssal hills using analytical theory, J. Geophys. Res., 118, 6303–6318, doi:10.1002/2013JC009212, 2013.

Mercier, H. and Colin de Verdiere, A.: Space and time scales of mesoscale motions in the eastern North Atlantic, J. Phys. Oceanogr., 15, 171–183, 1985.

Mourino, B., Fernandez, E., Etienne, H., Hernandez, F., and Giraud, S.: Significance of cyclonic SubTropical Oceanic Rings of Magnitude (STORM) eddies for the carbon budget of the euphotic layer in the subtropical northeast Atlantic, J. Geophys. Res., 108, 3383, doi:10.1029/2003JC001884, 2003.

Navarro-Pérez, E. and Barton, E. D.: Seasonal and interannual variability of the Canary Current, Sci. Mar., 65, 205–213, 2001.

New, A. L., Jia, Y., Coulibaly, M., and Dengg, J.: On the role of the Azores current in the ventelation of the North Atlantic Ocean, Prog. Oceanogr., 48, 163–194, 2001.

Nolasco, R., Cordeiro Pires, A., Cordeiro, N., and Dubert, J.: A high-resolution modeling study of the Western Iberian Margin mean and seasonal upper ocean circulation, Ocean Dynam., 63, 1041–1062, 2013.

Oliveira, P. B., Peliz, A., Dubert, J., Rosa, T. L., and Santos, A. M. P.: Winter geostrophic currents and eddies in the western Iberia coastal transition zone, Deep-Sea Res. Pt. I, 51, 367–381, 2004.

Onken, R.: The Azores Countercurrent, J. Phys. Oceanogr., 23, 1638–1646, 1993.

Owens, W. B. and Hogg, N. G.: Oceanic observations of stratified Taylor columns near a bump, Deep-Sea Res., 27, 1029–1045, 1980.

Paillet, J. and Mercier, H.: An inverse model of the eastern North Atlantic general circulation and thermocline ventilation, Deep-Sea Res. Pt. I, 44, 1293–1328, 1997.

Pedlosky, J.: Geophysical fluid dynamics, 2nd Edn., Springer, New York, 710 pp., 1987.

Pedlosky, J.: Ocean circulation theory, 2nd Edn., Springer, New York, 453 pp., 1998.

Pelegri, J. L., Arístegui, J., Cana, L., González-Dávila, M., Hernández-Guerra, A., Hernández-León, S., Marrero-Díaz, A., Montero, M. F., Sangrà, P., and Santana-Casiano, M.: Coupling between the open ocean and the coastal upwelling region off northwest Africa: water recirculation and offshore pumping of organic matter, J. Marine Syst., 54, 3–37, 2005.

Perez, F. F., Mintrop, L., Llinas, O., Glez-Davila, M., Castro, C. G., Alvarez, M., and Kortzinger, A.: Mixing analysis of nutrients, oxygen and inorganic carbon in the Canary Islands region, J. Marine Syst., 28, 183–201, 2001.

Pingree, R. D.: Ocean structure and climate (Eastern North Atlantic): in situ measurement and remote sensing (altimeter), J. Mar. Biol. Assoc. UK, 82, 681–707, 2002.

Pingree, R. D. and Le Cann, B.: Anticyclonic eddy X91 in the southern Bay of Biscay, May 1991 to February 1992, J. Geophys. Res., 97, 14353–14367, 1992.

Pingree, R. D. and Sinha, B.: Dynamic Topography (ERS-1/2 and sea truth) of subtropical ring (STORM 0 in the STORM Corridor (32–34° N), Eastern Basin, North Atlantic Ocean, J. Mar. Biol. Assoc. UK, 78, 351–376, 1998.

Pingree, R. D., Kou, Y. H., and Garcia-Soto, C.: Can Subtropical North Atlantic permanent thermocline be observed from space?, J. Mar. Biol. Assoc. UK, 82, 709–728, 2002.

Pollard, R. T. and Pu, S.: Structure and Circulation of the upper Atlantic ocean Northeast of the Azores, Prog. Oceanogr., 14, 443–462, 1985.

Pollard, R. T., Griffiths, M. J., Cunningham, S. A., Read, J. F., Perez, F. F., and Rios, A. F.: Vivaldi 1991 – a study of the formation, circulation and ventilation of Eastern North Atlantic Central Water, Prog. Oceanogr., 37, 167–192, 1996.

Read, J. F., Pollard, R. T., Miller, P. I., and Dale, A. C.: Circulation and variability of the North Atlantic Current in the vicinity of the Mid-Atlantic Ridge. Deep-Sea Res. Pt. I, 57, 307–318, 2010.

Reid, J. L.: On the middepth circulation and salinity field in the North Atlantic Ocean, J. Geophys. Res., 83, 5063–5067, 1978.

Richardson, P. L., McCartney, P. L., and Maillard, C.: A search for Meddies in historical data, J. Phys. Oceanogr., 15, 241–265, 1991.

Richardson, P. L., Bower, A. S., and Zenk, W.: A census of meddies tracked by floats, Prog. Oceanogr., 45, 209–250, 2000.

Rio, M. H., Guinehut, S., and Larnicol, G.: New CNES-CLS09 global mean dynamic topography computed from the combination of GRACE data, altimetry, and in situ measurements, J. Geophys. Res., 116, C07018, doi:10.1029/2010JC006505, 2011.

Roemmich, D. and Gilson, J.: The 2004–2008 mean and annual cycle of temperature, salinity, and steric height in the global ocean from the Argo Program, Prog. Oceanogr., 82, 81–100, 2009.

Schmidtko, S., Johnson, G. C., and Lyman, J. M.: MIMOC: A global monthly isopycnal upper-ocean climatology with mixed layers, J. Geophys. Res., 118, 1658–1672, 2013.

Shoosmith, D. R., Richardson, P. L., Bower, A. S., and Rossby, H. T.: Discrete eddies in the northern North Atlantic as observed by looping RAFOS floats, Deep-Sea Res. Pt. II, 52, 627–650, 2005.

Siedler, G. and Finke, M.: Long-period transport changes in the Eastern North Atlantic and their simulation by propagating waves, J. Geophys. Res., 98, 2393–2406, 1993.

Sparnocchia, S., Manzella, G. M., and La Violette, P. E.: The interannual and seasonal variability of the MAW and LIW core prop-

erties in the Western Mediterranean Sea, Coast. Estuar. Stud., 46, 177–194, 1994.

Stammer, D.: Global Characteristics of Ocean Variability Estimated from Regional TOPEX/POSEIDON Altimeter Measurements, J. Phys. Oceanogr., 27, 1743–1769, 1997.

Stramma, L. and Siedler, G.: Seasonal changes in the North Atlantic subtropical gyre. J. Geophys. Res., 93, 8111–8118, 1988.

Troupin, C., Machín, F., Ouberdous, M., Sirjacobs, D., Barth, A., and Beckers, J. M.: High-resolution climatology of the northeast Atlantic using Data-Interpolating Variational Analysis (Diva), J. Geophys. Res., 115, C08005, doi:10.1029/2009JC005512, 2010.

Volkov, D. L. and Fu, L. L.: On the Reasons for the Formation and Variability of the Azores Current, J. Phys. Oceanogr., 40, 2197–2220, 2010.

WOA13: World Ocean Atlas, available at: http://www.nodc.noaa.gov/OC5/ (last accessed: 1 December 2014), edited by: Levitus, S. and Mishonov, A., temperature compiled by: Locarnini, R. A., Mishonov, A. V., Antonov, J. I., Boyer, T. P., Garcia, H. E., Baranova, O. K., Zweng, M. M., Paver, C. R., Reagan, J. R., Johnson D. R., Hamilton, M., and Seidov, D. (NOAA Atlas NESDIS 73, 2013) and salinity compiled by: Zweng, M. M, Reagan, J. R., Antonov, J. I., Locarnini, R. A., Mishonov, A. V., Boyer, T. P., Garcia, H. E., Baranova, O. K., Johnson, D. R., Seidov, D., and Biddle, M. M., (NOAA Atlas NESDIS 74, 2013).

WOA09: World Ocean Atlas 2009, available at http://www.nodc.noaa.gov/OC5/WOA09/pubwoa09.html, temperature compiled by Locarnini, R.A., A.V. Mishonov, J.I. Antonov, T.P. Boyer, H.E. Garcia, O.K. Baranova, M.M. Zweng, and D.R. Johnson, 2010. *World Ocean Atlas 2009, Volume 1: Temperature.* S. Levitus, Ed. NOAA Atlas NESDIS 68, U.S. Government Printing Office, Washington, D.C., 184 pp., and salinity compiled by Antonov, J.I., D. Seidov, T.P. Boyer, R.A. Locarnini, A.V. Mishonov, H.E. Garcia, O.K. Baranova, M.M. Zweng, and D.R. Johnson, 2010. *World Ocean Atlas 2009, Volume 2: Salinity.* S. Levitus, Ed. NOAA Atlas NESDIS 69, US Government Printing Office, Washington, D.C., 184 pp., 2009.

WOD, World Ocean Database. Boyer, T.P., J.I. Antonov, O.K. Baranova, C.Coleman, H.E. Garcia, A.Grodsky, D.R. Johnson, R.A. Locarnini, A.V. Mishonov, T.D. O'Brien, C.R. Paver, J.R. Reagan, D. Seidov, I.V. Smolyar, M.M. Zweng, 2013, World Ocean Database 2013. Sydney Levitus, Ed.; A. Mishonov, Technical Ed.; NOAA Atlas NESDIS 72, 209.